Geo-archaeological records of large Holocene tsunamis along the hyperarid coastal Atacama Desert in the major northern Chile seismic gap

Tomás León [a], [**], Gabriel Vargas [a], [*], Diego Salazar [b], James Goff [c], Jean Louis Guendon [d], Pedro Andrade [e], Gabriel Alvarez [f]

[a] Departamento de Geología, Facultad de Ciencias Físicas y Matemáticas, Universidad de Chile, Plaza Ercilla 803, Santiago, Chile
[b] Departamento de Antropología, Universidad de Chile, Ignacio Carrera Pinto 1045, Piso 2, Ñuñoa, Santiago, Chile
[c] Pangea Research Centre, School of Biological, Earth and Environmental Sciences, University of New South Wales, Sydney 2052, Australia
[d] Aix Marseille Université, CNRS, MCC, LAMPEA UMR 7269, 13094, Aix-en-Provence, France
[e] Carrera de Antropología, Facultad de Ciencias Sociales, Universidad de Concepción, Victor Lamas 1290, Concepción, Chile
[f] Departamento de Ingeniería en Geomensura y Geomática, Facultad de Ingeniería, Universidad de Antofagasta, Avenida Universidad de Antofagasta 02800, Antofagasta, Chile

ABSTRACT

The coastal Atacama Desert is exposed to strong earthquakes and giant tsunamis associated with the subduction of the Nazca plate beneath the South American plate. Nevertheless, historical and geological records of tsunamis and paleotsunamis in this region are scarce. Taltal (25.4°S) is located at the southern edge of the hyperarid Atacama Desert within a major historical ~1000 km-long megathrust seismic gap in northern Chile where the most recent large tsunamigenic earthquakes occurred in 1877 CE and 1922 CE, rupturing its northern and southern segments, respectively. By multiproxy geological and archaeological analyses from pits and trenches, we report distinctive strata of reworked archaeological material as well as sedimentary layers that we interpret as being produced by tsunami run-up and/or backwash deposition. We identified two large Holocene paleotsunamis dated close to ~4000 cal yrs BP and younger than 863 ± 199 CE (~1087 cal years BP). By comparing the run-ups of the last historical tsunamis with our minimum run-up estimates from the geo-archaeological record, we conclude that the impact of these Holocene paleotsunamis was larger than any known historical event, suggesting the need to re-evaluate local, regional and Pacific basin-scale tsunami hazard assessments.

© 2019 Elsevier Ltd. All rights reserved.

1. Introduction

The hyperarid Atacama Desert in northern Chile is adjacent to the subduction contact between the Nazca and South American plates. Convergence at this tectonic margin occurs in a northeasterly direction at a rate of around 67 mm/yr, subjecting the adjacent coasts to strong earthquakes and giant tsunamis (Angermann et al., 1999; Schurr et al., 2014; Ruiz and Madariaga, 2018, Fig. 1). Taltal (25.4°S), is located within a major historical ~1000 km-long seismic gap encompassing the Atacama Desert's coasts between ~18.5°S

and ~29°S, in a region characterized by a highly coupled interplate subduction contact as deduced from geodetic measurements (Métois et al., 2016, Fig. 1), and where only limited ruptures have occurred since the end of the 19th century and the beginning of the 20th century (Comte and Pardo, 1991; Ruiz and Madariaga, 2018). Along this major seismic gap region the last large tsunamigenic earthquakes were the M_w ~8.8 1877 CE and the M_w ~8.5 1922 CE events, whose rupture areas occurred along its northern and southern segments, respectively (Comte and Pardo, 1991; Ruiz and Madariaga, 2018, Fig. 1). While the relatively short historical record of earthquakes and tsunamis is well established, it largely comprises evidence from the last two centuries (Comte and Pardo, 1991; Ruiz and Madariaga, 2018, Fig. 1) and little is known about prehistoric events in this seismic gap. This is at odds with evidence reported from areas characterized by a more humid climate such as

* Corresponding author.
** Corresponding author.
 E-mail addresses: tleon@ing.uchile.cl (T. León), gvargas@ing.uchile.cl (G. Vargas).
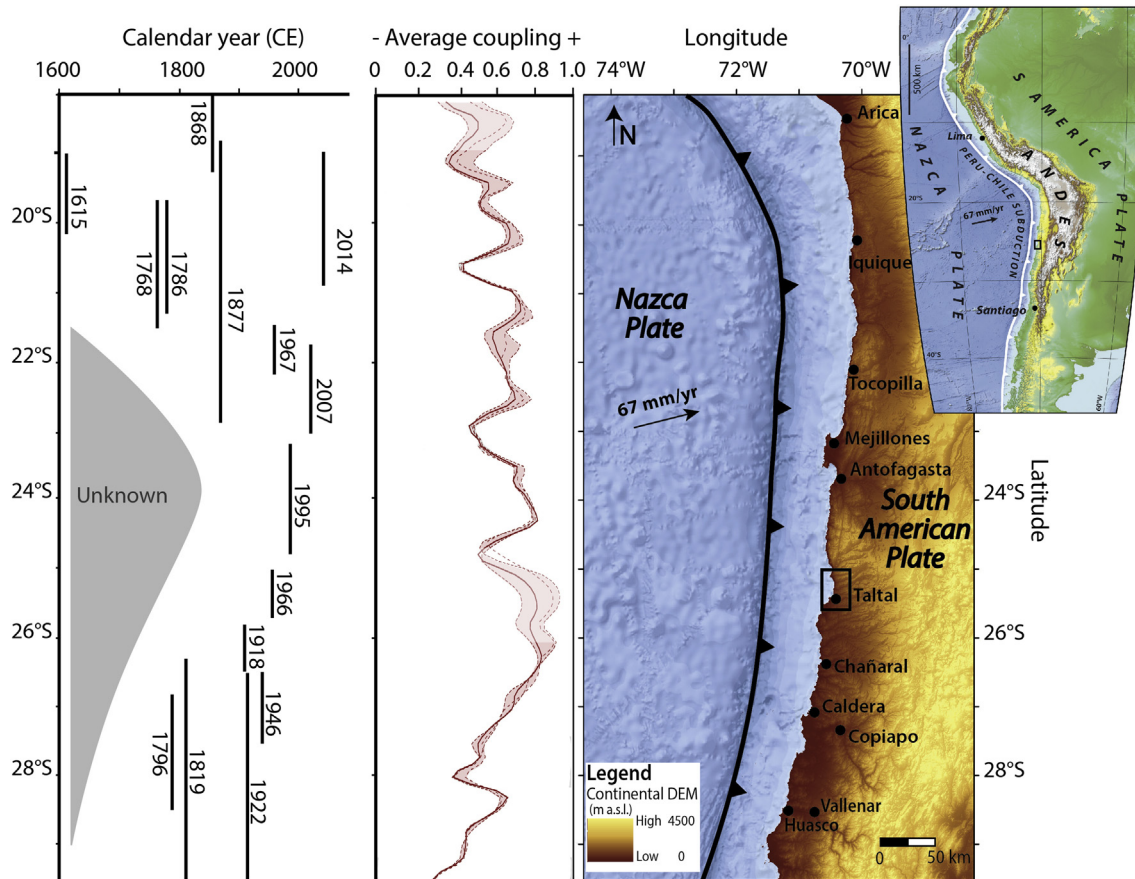
Fig. 1. Convergence tectonic contact of the Nazca beneath the South American plates along northern Chile. Taltal is situated within a major seismic gap region characterized by a highly coupled interplate subduction contact (Angermann et al., 1999; Comte and Pardo, 1991; Métois et al., 2016; Ruiz and Madariaga, 2018).

central-southern Chile, where environmental conditions favor the formation of wetlands, lagoons and estuarine systems with ample accommodation space for the preservation of tsunami deposits (Cisternas et al., 2005; Ely et al., 2014; Dura et al., 2017). Unlike this last region, the coast of northern Chile comprises steep cliffs, rocky uplifted platforms, narrow coastal plains and a hyperarid climate (less than 1 mm of rainfall per year in the core of the hyperarid coastal Atacama Desert), providing unfavorable conditions for the preservation of both historical and paleotsunami deposits. Moreover, the preservation and identification of paleotsunami deposits is further hampered by the occurrence of infrequent, but sporadic, heavy rainfall that occurs during moderate to strong El Niño events causing significant debris and mud flows (Vargas et al., 2000, 2006), as well as by the occurrence of sporadic storms that can inundate the coast (Carvajal et al., 2017).

Sudden coseismic vertical changes adjacent to subduction zones may create a series of distinctive sharp lithologic contacts and geomorphological features such as uplifted marine terraces and beach-ridges or subsidence wetlands (Plafker and Savage, 1970; Atwater, 1987; Farías et al., 2010; Vargas et al., 2011) that can provide important paleoseismic records over thousands of years (Plafker et al., 1992; Nelson et al., 1996; Witter et al., 2003; González-Alfaro et al., 2018). In addition, widespread sand beds deposited by tsunamis following great earthquakes can often be found in association with such geomorphologic evidence of sudden relative sea level changes (Sawai, 2001; Kelsey et al., 2002; Cisternas et al., 2005; Satake and Atwater, 2007). On Mejillones peninsula just to the north of the Taltal region (Fig. 1), precise

radiocarbon dating and geomorphological analysis of emerged littoral deposits indicate coastal uplift rates in the order of 1.4—1.7 m/ka since Marine Isotopic Stage 3 (MIS 3), i.e. in the last ~44 ka (González-Alfaro et al., 2018). Geomorphological and chronological evidence from emerged Holocene littoral deposits confirm these uplift rates, suggesting the importance of large megathrust earthquakes in the coastal uplifting process (González-Alfaro et al., 2018), and by association the potential for tsunami-genesis along the northern Chile seismic gap region.

Taltal is situated to the south of the rupture segment of the M_w~8.8 1877 CE megathrust (Fig. 1), which generated a giant tsunami that inundated much of the region. The rupture encompassed at least 500 km of the subduction interplate contact between Pisagua-Iquique and Mejillones (~20-23°S; Kausel, 1986; Comte and Pardo, 1991; Ruiz and Madariaga, 2018, Fig. 1). This rupture generated a Pacific-wide tsunami, which caused run-up in the order of 15—21 m along coastlines adjacent to the rupture zone (Kausel, 1986; Comte and Pardo, 1991; Ruiz and Madariaga, 2018), and tsunami heights of 2.4—3.0 m on distant Japanese shores (Tsuji, 2013). Despite historical accounts of high tsunami run-ups in 1877 CE, geological evidence of this event and its predecessors have never been recorded along the Atacama coastline. Notwithstanding the above, submarine slump deposits and an associated erosional basal contact preserved in laminated sediments off Mejillones Bay (23°S), suggest that a predecessor of the major 1877 CE event probably occurred around 1409—1449 CE (1429 ± 20 CE; Vargas et al., 2005). This probably corresponds with an historically-documented distant tsunami that struck the Japanese coasts on

September 7, 1420 CE (Tsuji, 2013; Ruiz and Madariaga, 2018). Moreover, coastal boulder deposits found in the southern segment of the Atacama region 250 km south of Taltal (within the rupture area of the 1922 CE earthquake) have been dated to around 1300—1600 CE and as such provide evidence for this 1420 CE event (Abad et al., 2019, Fig. 1). However, the coasts around Taltal-Paposo area (Fig. 2) have no historical or prehistoric records of large tsunamigenic megathrust earthquakes and as such, this region constitutes one of the most poorly understood seismic gap segments in the world (Métois et al., 2016, Fig. 1).

Archaeological research in the Taltal area has revealed an occupational history extending back to the early Holocene (since at least ca. 11700 cal years BP) by the Huntelauquén Cultural Complex (Salazar et al., 2018). Nonetheless, most of the coastal archaeological record encompasses the mid to late Holocene period (Béarez et al., 2016; Rebolledo et al., 2016; Salazar et al., 2015), following global sea level stabilization around 6700-4200 years ago (Lambeck et al., 2014). Dozens of archaeological sites have been recorded by systematic surveys along the Taltal-Paposo

coastal zone (Salazar et al., 2015, Fig. 2), making them potentially important locations for the study of paleotsunami inundation of the region.

Bearing in mind the wealth of archaeological data and early historical evidence for past tsunamis, we adopted a multiproxy approach to study Holocene paleotsunami deposits in the Taltal region. We employed archaeological, geomorphological, sedimentological, mineralogical, stratigraphical, paleontological, geochemical and geochronological techniques to document two potential instances of tsunami inundation. We compared minimum run-up estimates from these inferred paleotsunami deposits with a reanalysis of historical records of tsunami impacts in Taltal, proposing that Holocene paleotsunamis struck the region more severely than any recorded historical event.

2. Site and methods

Siliciclastic coastal environments represent a challenge for the identification of distinctive deposits laid down by tsunamis (Spiske
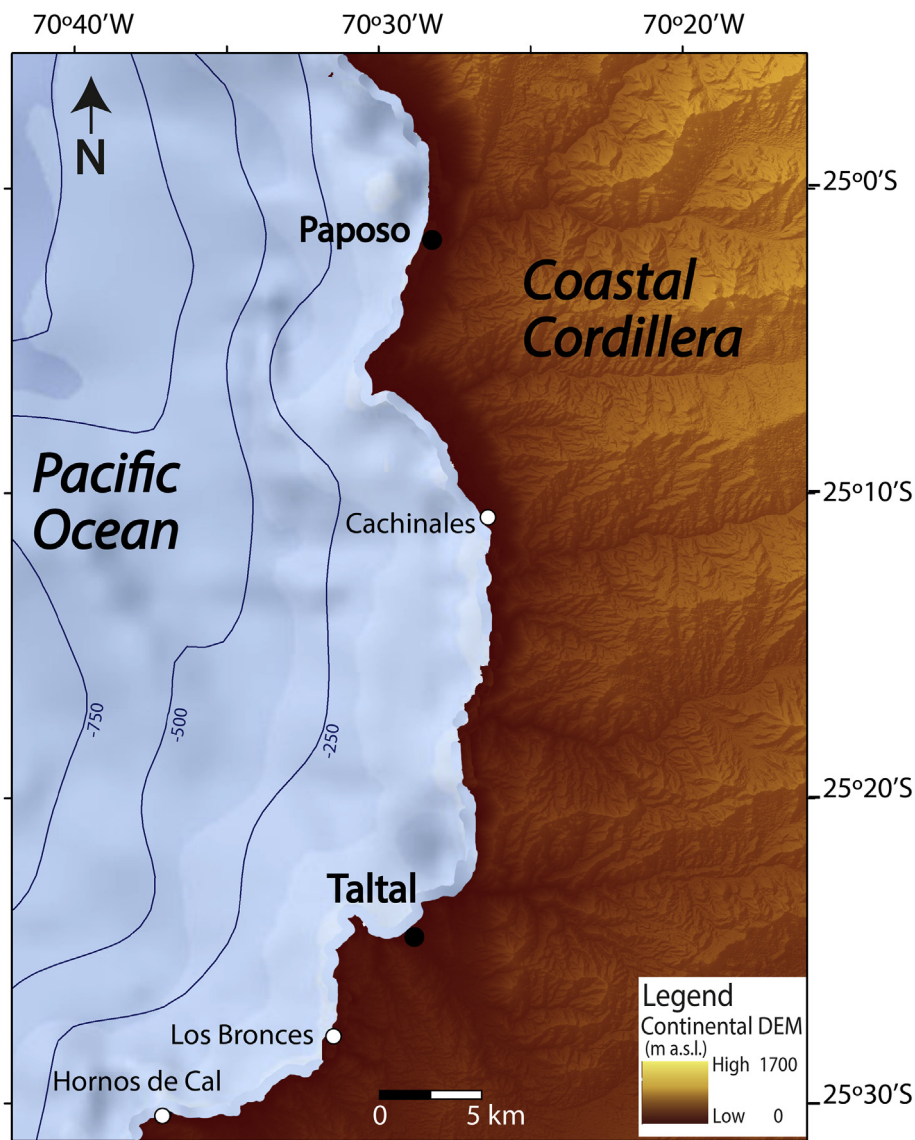
Fig. 2. Geomorphological context and location of study sites in the Taltal-Paposo area of northern Chile. Contour lines indicate isobaths of −250, −500 and −750 m b.s.l. The Coastal Cordillera rises up to ~2000 m a.s.l. and is mostly drained by local ravines not connected with the main Andes Cordillera.

et al., 2013; Bahlburg et al., 2017). Because of the hyperarid climate characterizing the mostly rocky coasts of the Atacama Desert along northern Chile, runoff is minimal, with exception of sporadic, heavy rainfall during El Niño events, thus limiting the development of wetlands, lagoons or estuarine systems that could provide accommodation space for onshore-coastal deposition of tsunami sediments. We therefore adopted a multiproxy geo-archaeological approach with which to evaluate the possible tsunamigenic character of sedimentary deposits in the Taltal-Paposo coastal region (Fig. 2; e.g. Cisternas et al., 2005; Goff et al., 2012; Cain et al., 2019), from Cachinales beach (Fig. 3), Los Bronces and Hornos de Cal archaeological sites (Figs. 4 and 5).

The Cachinales beach site is situated to the north of Taltal (Fig. 2) in a natural (non-archaeological) trench located up to 9 m a.s.l. and 150 m from the coast (Fig. 3). The Los Bronces archaeological site is located to the south of Taltal (Fig. 2), in a narrow coastal plain and close to a ravine subject to sporadic alluvial sedimentation. Here we dug two trenches located at 8 and 9 m a.s.l. and 120 m from the coast, at approximately 50 m from a middle to late Holocene archaeological site (Fig. 4). At the Hornos de Cal archaeological site the search for potential tsunami deposits was limited to the area encompassed by cultural remains. We dug two trenches located at 10 and 11 m a.s.l., respectively, and 100 m from the coast (Fig. 5).

All of the sites are situated on uplifted terraces or coastal plains surrounded by rocky outcrops that served to protect the deposits and shell midden from erosion caused by active terrestrial and coastal processes. The lithology, color and stratigraphy of all of the trenches and pits were described in the field. Fifty-nine samples were collected for sedimentological, mineralogical, geochemical, biological and archaeological analyses from Cachinales, Los Bronces and Hornos de Cal sites (Appendices A and B).

Sedimentological analyses were carried out on 31 samples from Los Bronces and 13 from Hornos de Cal. Manual sieving was carried out using eight different sieve sizes (4000, 2000, 1000, 500, 250, 125 and 75 μm) with laser grain size analyses of the finer material using a Malvern Mastersizer 2000. The results were processed with GRADISTAT 8.0 software (Blott and Pye, 2001) and presented using Folk and Ward (1957) criteria. Sediment texture was determined using a stereoscopic microscope to identify the roundness, sphericity and mineralogical components of the sediments, with the aim of determining their textural and compositional maturity. X-ray fluorescence (XRF) analyses were carried out using a Shimadzu EDX-720. X-ray diffraction (DRX) and Fourier Transformed InfraRed (FTIR) mineralogical analyses were carried out to identify mineralogical phases and to characterize changes in the mineralogical composition from sediment samples (Bertaux et al., 1998).

Archaeological organic material was analyzed to differentiate between anthropogenic and non-anthropogenic sources. Mollusk shells were identified from the coarse sieve fraction of the samples (>2000 μm). Identification and interpretation were carried out

using a descriptive catalogue of nearshore mollusks (gastropods and bivalves) from the Antofagasta area (23°S) that provided information such as habitat depth range and morphological characteristics (Guzmán et al., 1998). The medium to fine grain size fraction of the samples (1000, 500 and 250 μm) were analyzed under a stereoscopic microscope with the aim of identifying small gastropods typical of intertidal rocky environments, as well as to determine variations in fish bone-content diagnostic of local archaeological deposits.

AMS (Accelerator Mass Spectrometry) radiocarbon analyses were carried out on shells and charcoal fragments to provide geochronological determinations from within or close to distinctive sedimentary layers (Table 1). Sixteen samples were analyzed at the Center for Applied Isotopes Studies at the University of Georgia and at DirectAMS Radiocarbon Dating Service. Conventional radiocarbon results from marine shell samples were calibrated considering previous regional marine reservoir effect estimates from northern Chile (Ortlieb et al., 2011).

Geomorphological context and field observations were complemented through photogrammetric analyses using high-resolution images taken with a Phantom 4 Pro drone, with an average of 350 photos from each site. These images were processed to generate Digital Elevation Models (DEM), ortho-photographs and 3D models. The elevation and the distance of each study site with respect to the shoreline were measured using a barometric GPS and by examining the 3D models constructed by photogrammetry. Precise geodetic profiles obtained by Differential Global Positional System (DGPS) measurements served to calibrate the DEMs and 3D models, as well as to precisely estimate the location of mean sea level at each site, through the use of tide tables and procedures determined by the Chilean Navy Hydrographic Service (SHOA). Specifically, we obtained the sea level height from daily observations at the Antofagasta main port (Puerto Patron), with corrections for Paposo and Taltal secondary ports (Fig. 2). Once the time and sea level heights were corrected for the secondary ports we calculated the level sea-zero and used a total station to obtain the precise location of each measured point, with millimeter precision. Thus, we obtained altimetry and DEMs calibrated with respect to the mean sea level position at each site, with a precision of ±10 cm.

Finally, we recovered and reanalyzed information from local and regional newspapers related to the last two large historical tsunamis that affected the region in 1877 CE and 1922 CE. Data of tsunami inundation from newspaper chronicles served to reanalyze the impact of these last two episodes in the study region, by comparing this information with the official Tsunami Inundation Maps (CITSU) produced by SHOA and with our new study data. These data were used to inform our discussion about the implications of our findings for tsunami hazard assessment in the study area as well as for the Pacific Ocean basin.

Fig. 3. Local geomorphological context of Cachinales beach, showing the location of the site studied for paleotsunami research (see location in Fig. 2).
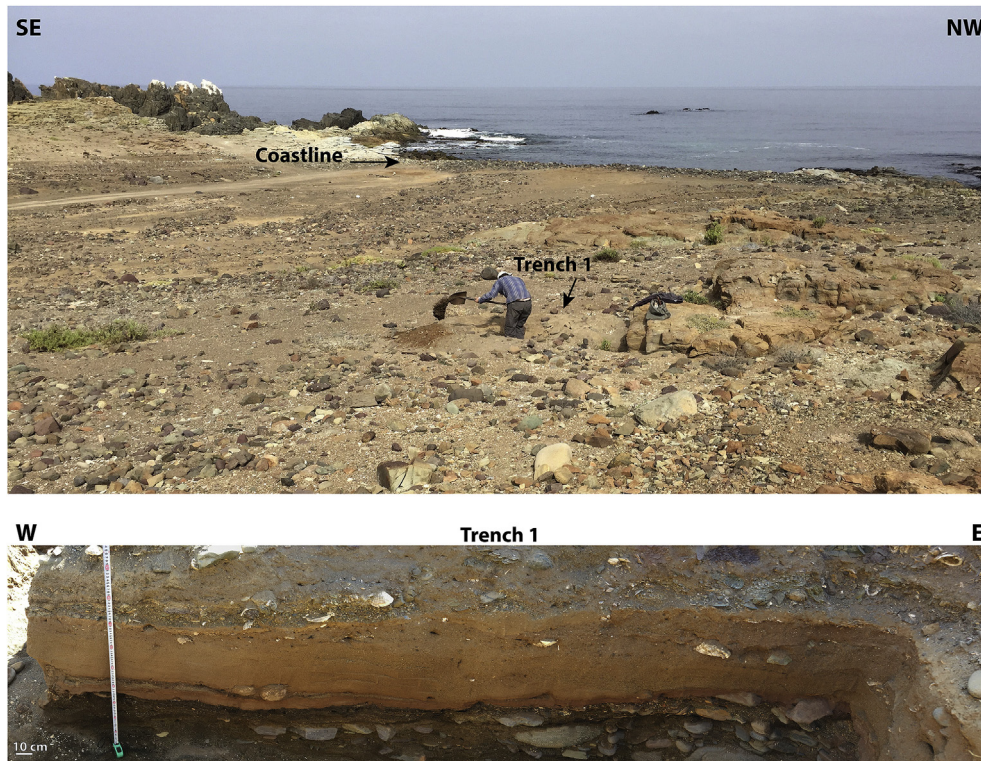
Fig. 4. Local geomorphological context of Los Bronces site (above), showing the trench studied for paleotsunami research (below; see location in Fig. 2).

Fig. 5. Local geomorphological context of Hornos de Cal archaeological site, showing the position of the trenches studied for paleotsunami research (see location in Fig. 2).

3. Results and interpretation

3.1. Reanalysis of the impact of large historical tsunamis

According to our reanalysis of historical information (Table 2), in the last ~ two centuries Taltal has been affected by large tsunamis following the Iquique 1877 CE and Vallenar 1922 CE megathrust earthquakes. The Taltal 1966 CE megathrust caused only small tidal variations similar to the 1995 CE M_w 8.0 Antofagasta earthquake that only produced a small tsunami affecting the coast around the Mejillones Peninsula-Antofagasta area (Ruiz and Madariaga, 2018). In order to assess the regional extent of the 1877 CE and 1922 CE events, we reanalyzed the effects of these tsunamis in cities situated along and beyond the major seismic gap of northern Chile, between Coquimbo and Arica (Fig. 1; Table 2). The impact of these events on coastal locations is summarized below:

- **Iquique, May 9**th, **1877 CE**: According to some authors (Comte and Pardo, 1991; Ruiz and Madariaga, 2018) this tsunamigenic

megathrust is one of the largest historical events of southern Peru and northern Chile. Its magnitude was estimated as M_w ~8.6—8.8, with 400—500 km of rupture length and with an epicentral area adjacent to the coast between Iquique and the northern edge of the Mejillones peninsula (Kausel, 1986; Comte and Pardo, 1991; Ruiz and Madariaga, 2018). According to our review of chronicles and previous publications (Table 2), it caused tsunami run-ups in the order of 19 m in Arica, 20 m in Iquique, 22 in Mejillones, 12 m in Antofagasta, 7 m in Chañaral and 6 m in Coquimbo among others with a marked decrease from the Mejillones peninsula southward (Table 2). In Taltal, tsunami inundation penetrated about 160 m inland from the coastline with up to 7 m run-up (Table 2).

- **Vallenar, November 11**th, **1922 CE**: This earthquake ruptured ~300 km of the subduction interplate contact in the Atacama region along the southern portion of the major seismic gap of northern Chile, with an estimated magnitude of Ms ~8.3—8.5 (Beck et al., 1998). It generated a tsunami that struck the coast of South America from Callao, in Peru, to Coquimbo, in Chile, with

Table 1
Radiocarbon dates from trenches within the study area (see Figs. 7, 10 and 13 for stratigraphic positions of individual samples).

Field ID sample	Laboratory ID	Site	Material dated	δ13C (‰)	Conventional Radiocarbon Age (14C yr BP)	ΔR*	Calibrated Age Range (2σ) (cal yrs BP)**
T1620A	UGAMS 31151	Cachinales	Shell (*Concholepas ch.*)	0.88	4860 ± 20	226 ± 98	4859 (4575–5142)
T1620B	D-AMS 032930	Cachinales	Shell (*Fissurella sp.*)	8.50	6179 ± 36	226 ± 98	6397 (6172–6622)
T1621	UGAMS 31152	Cachinales	Shell (*Concholepas ch.*)	−0.03	2400 ± 20	226 ± 98	1761 (1523–1999) 189 CE (50 BC–427 CE)
T1627	UGAMS 31154	Los Bronces	Shell (*Tegula sp.*)	2.91	4260 ± 20	226 ± 98	4086 (3804–4369)
T1628	UGAMS 31155	Los Bronces	Charcoal	−21.96	3880 ± 25	0	4326 (4240–4412)
T1629	UGAMS 31156	Los Bronces	Shell (*Fisurella sp.*)	1.72	4240 ± 20	226 ± 98	4048 (3760–4336)
T1630	UGAMS 31157	Los Bronces	Shell (*Concholepas ch.*)	−0.48	4210 ± 20	226 ± 98	3990 (3704–4275)
T1631	UGAMS 31158	Los Bronces	Shell (*Concholepas ch.*)	0.47	4250 ± 20	226 ± 98	4063 (3777–4349)
T1632	UGAMS 31159	Los Bronces	Shell (*Concholepas ch.*)	1.09	4200 ± 20	226 ± 98	3975 (3691–4258)
T1633	UGAMS 31160	Los Bronces	Shell (*Concholepas ch.*)	0.44	4190 ± 20	226 ± 98	3963 (3681–4244)
T1634	UGAMS 31161	Los Bronces	Charcoal	−18.00	3930 ± 25	0	4362 (4287–4437)
T1635A	UGAMS 31162	Los Bronces	Shell (*Concholepas ch.*)	2.05	2160 ± 20	226 ± 98	1498 (1281–1715) 452 CE (235–669 CE)
T1635B	D-AMS 032931	Los Bronces	Shell (*Concholepas ch.*)	11.60	1757 ± 29	226 ± 98	1087 (888–1286) 863 CE (664–1062 CE)
TA 1705	UGAMS 31192	Hornos de Cal	Charcoal	−17.62	5560 ± 25	0	6339 (6278-6399)
TA1710A	UGAMS 31193	Hornos de Cal	Charcoal	−21.67	3990 ± 20	0	4491 (4464–4518)
TA1710B	UGAMS 31194	Hornos de Cal	Shell (*Fisurella sp.*)	0.94	5750 ± 25	226 ± 98	5921 (5675–6166)
JL-HCAL	D-AMS 024529	Hornos de Cal	Charcoal	-27.1	3883 ± 29	0	4279 (4150–4408)

* Ortlieb et al. (2011), **Stuiver et al. (2018).

the port of Chañaral being most affected (Beck et al., 1998). Based on historical information and chronicles, Lomnitz (2004) inferred tsunami heights as high as 9-7 m in the cities of Cha-ñaral, Caldera and Coquimbo (Table 2). Our review of historical information suggests high tsunami run-ups in the coastal cities located adjacent to the epicenter, and decreasing markedly in elevation to the north and south, with 10 m in Coquimbo, 12 m in Huasco, 9 m in Chañaral and 2 m in Arica (Table 2). In Taltal, the tsunami flooded 50 m from the coastline and reached up to 5 m run-up (Table 2).

- **Taltal, December 28th, 1966**: The magnitude of this event was estimated as M$_w$ ~7.7, with an epicenter located in the ocean to the south of the city of Taltal. According to Deschamps et al. (1980), the megathrust rupture encompassed the deeper portion of the interplate subduction contact. Historical information reviewed from chronicles confirms that this earthquake did not generate any large tsunami in the Taltal area (Table 1). Only slight sea level variations were recorded in the harbor associated with waves that flooded the beach. An even smaller effect can be inferred for the 1995 Antofagasta earthquake that ruptured to the north of Taltal (Delouis et al., 1997).

3.2. Geo-archaeological tsunami records in the Taltal coastal region

3.2.1. Cachinales profile

This site is located to the north of Taltal, 17 km to the south of Paposo (Fig. 2). It is on an uplifted coastal platform adjacent to a 2.7 km long and 0.2 km wide beach with a N35°W oriented coast-line (Fig. 6). Here we found a distinctive brownish deposit (CHC-B) consisting of rounded gravels embedded in a sandy matrix. This was observed along the sidewall of a northeast-southwest oriented drainage channel located 8 m a.s.l. and 120 m from the coastline. It

could be traced inland up to 9 m a.s.l. and 150 m from the coast (Fig. 7). At the base of the profile was a 55 cm thick layer (CHC-A; Figs. 7 and 8) of angular gravel and pebbles chaotically embedded within a medium to fine sandy matrix. The sandy matrix is comprised of subangular clasts of quartz and carbonates together with lithic fragments characterized by a medium sphericity. Layer CHC-A is interpreted as alluvial reworking of littoral sediments.
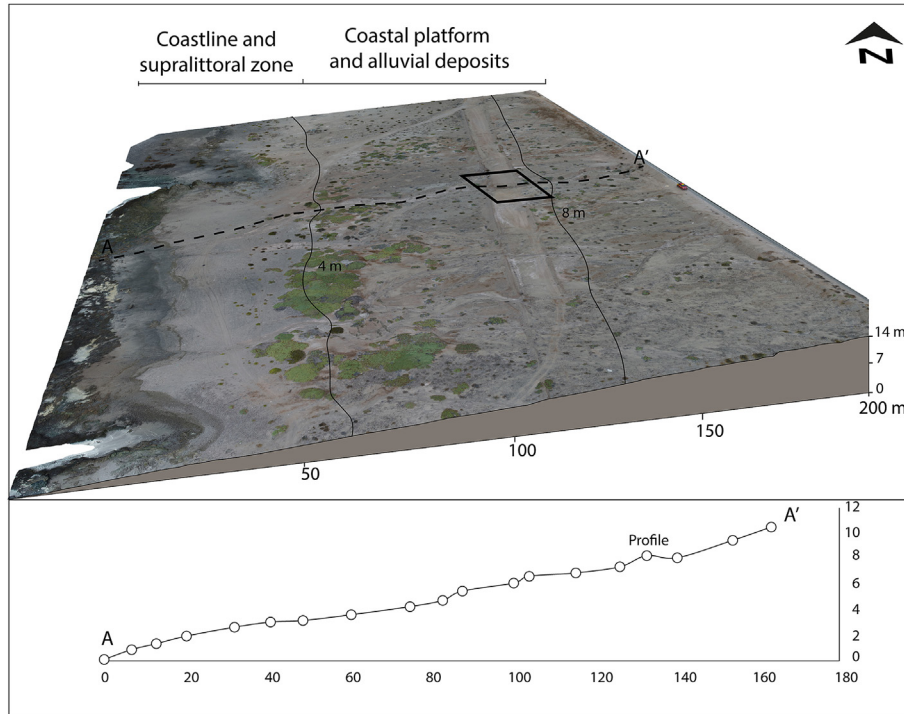
Layer CHC-A has a sharp, irregular upper contact with a 45 cm thick deposit of well-rounded gravel embedded within a medium to fine sandy matrix of subangular and rounded particles that fines inland (CHC-B; Figs. 7a and 8a). The gravel clasts exhibit a south-easterly imbrication (mean value of N149°, N = 21) suggesting deposition by water flowing from the northwest towards the southeast, i.e. roughly parallel to the coastline (Fig. 7b and d). This clasts-imbrication differs markedly from the dominant wind di-rection that drives storm waves from the southwest. The layer comprises a large quantity of shells, root fragment, lithic clasts and quartz grains within the matrix. The conspicuous basal erosional contact has associated rip-up clasts in the lower section on layer CHC-B (Fig. 8b) and material injected downwards into the under-lying sediments (CHC-A) (Fig. 8a). We interpret these as evidence for high-energy inundation and possible liquefaction during sedi-mentary deposition (Fig. 8). These data indicate the deposition of sediments from an unusually high-energy event that inundated from the northwest, i.e. from the sea. The well-rounded clasts contained within the deposit are also consistent with those found today on the modern beach (Fig. 7c). We infer deposition here as the result of tsunami inundation.

The top of the profile at Cachinales is defined by a 20 cm thick layer of poorly sorted and low sphericity sub-angular clasts chaotically dispersed within a medium to fine sandy matrix composed of angular sediments. This has a sharp, irregular lower contact with CHC-B and is interpreted as an alluvial layer.

Table 2
Summary of information about the impact of the 1877 CE and 1922 CE tsunamis in principal cities along the coast of northern Chile, including coastal run-up estimates.

Tsunami episode	Source/Edition	Locality	Cites	Run-up (m)
1877	El Diario Oficial/Santiago, May 11, 1877.	Chañaral	"Big wave rose 50–100 m from the shoreline"	6
	El Diario Oficial/Santiago, May 15, 1877.	Pisagua	"The sea came out 17 feet"	5
	La Reforma/Serena, May 11, 1877.	Coquimbo	"Reached the dock"	6
	La Reforma/Serena, May 14, 1877.	Antofagasta	"Destroyed … the best of the commerce"	2
	La Reforma/Serena, May 16, 1877.	Iquique	"Water rose about 6 feet on the walls of the customs"	2
		Antofagasta	"It's was invaded by the water in the Ballivian passage"	6
		Mejillones	"Since post office to Chilean customs"	15
	La Reforma/Serena, May 18, 1877.	Iquique	"The sea has razed part of railway station"	6
		Cobija	"The carts that were on the beach have appeared 3 ½ block of distance"	18
	"Narraciones históricas de Antofagasta". El terremoto y salida de mar del 9 de mayo de 1877/Isaac Arce (1930/1997).	Antofagasta	"The sea has reach to the center of Colón square"	6
	Silgado (1985).	Chañaral	"Big surges flooded the best buildings"	7
		Arica	"The one at 4 a.m. it was the biggest wave with a height of 40–45 feets"	14
		Pisagua	"The sea reached 50 m"	5
		Caldera	"Bay flooded up to a height of 2.5–3 m"	3
	Barros (2010).	Iquique	"The sea flooded from the Puntilla until the Morro"	3
	Geinitz (1878/2010)			
		Mejillones	"The low part of the city was swallowed by the sea"	7–11.5
	Fuchs (1878).	Iquique	"Inundation had a height of 20 m"	20
	Cruz (1966)	Mejillones	"The wave reaches a height of 22 m"	22
	Galaz-Mandakovic, D. & E. Owen (2015)	Tocopilla	"The rest of the city … was swept by the sea"	10
	SHOA (2010).	Arica	Historic tsunami records by SHOA	18
		Iquique	Historic tsunami records by SHOA	21
		Cobija	Historic tsunami records by SHOA	6–9
		Mejillones	Historic tsunami records by SHOA	9
		Caldera	Historic tsunami records by SHOA	11
	SHOA (CITSU).	Tocopilla	Tsunami inundation chart, CITSU	20
		Mejillones	Tsunami inundation chart, CITSU	18
		Antofagasta	Tsunami inundation chart, CITSU	12
		Taltal	Tsunami inundation chart, CITSU	7
1922	La Razón/Taltal, November 11, 1922.	Chañaral	"A sea surge, flooding almost the entire dock"	9
		Antofagasta	"The sea reached Balmaceda street."	6
		Taltal	"The sea rose up to six feets"	2
	La Razón/Taltal, November 13, 1922.	Chañaral	"The sea rose more than 9 m above the sea level"	9
		Antofagasta	"The army radiotelegraphy office was completely devastated by the sea"	9
	La Razón/Taltal, November 22, 1922.	Chañaral	"This water advance step over the hospital"	11
	El Imparcial/Taltal, November 11, 1922.	Taltal	"The sea flooded the dock beach"	2
	La voz del Pueblo/Taltal, November 11, 1922.	Taltal	"Covering only 50 m from the beach"	5
	Boletín del Servicio Sismológico de Chile XVI. Terremoto de Atacama/1922.	Antofagasta	"Flooding the passengers dock … some houses of Brasil avenue"	5
		Taltal	"The tsunami took eight boats"	2
		Chañaral	"More than 1 km was flooded"	11
	La Tarde/Coquimbo, November 11, 1922.	Coquimbo	"A lot of residents in Baquedano avenue died by the shock of the waves"	7
	El Comunista/Antofagasta, November 14, 1922.	Coquimbo	"Victoria's suburb was devastated by the sea"	7
	El Comunista/Antofagasta, November 18, 1922.	Coquimbo	"Customs stand was deposited in Aldunate street"	5–10
	El Mercurio de Antofagasta/Antofagasta, November 11, 1922.	Antofagasta	"Some houses of Brasil avenue were flooded"	5
	El Mercurio de Antofagasta/Antofagasta, November 12, 1922.	Antofagasta	"The sea flooded about 3 km"	9
		Chañaral	"Post office totally destroyed"	9
		Huasco	"Boats were in a forest two km from Huasco in Bellavista farm"	12
	El Mercurio de Antofagasta/Antofagasta, November 13, 1922.	Caldera	"The sea rose 8 m"	8
		Huasco	"From the shoreline, the sea extended half a league"	12
	El Mercurio de Antofagasta/Antofagasta, November 15, 1922.	Huasco	"The tsunami destroyed … N°3 School"	7
	El Mercurio de Antofagasta/Antofagasta, November 19, 1922.	Antofagasta, La Chimba	"Hitting the first houses"	9
	El Mercurio de Antofagasta/Antofagasta, November 20, 1922.	Coquimbo	"The sea reached the railway line in La Serena"	7
	Sismos y Tsunamis/SHOA (2010).	Caldera	Historic tsunami records by SHOA	6
		Chañaral	Historic tsunami records by SHOA	9
		Coquimbo	Historic tsunami records by SHOA	5
	SHOA (CITSU).	Taltal	Tsunami inundation chart, CITSU	7
		Chañaral	Tsunami inundation chart, CITSU	15
		Huasco	Tsunami inundation chart, CITSU	10
		Coquimbo	Tsunami inundation chart, CITSU	7
1966	La Prensa de Tocopilla, Tocopilla, December 29, 1966	Taltal	"The tide gauge didn't show any alteration at this port"	0
	Diario El Día, La Serena, December 30, 1966	Taltal	"It was reported that the sea in Taltal is quiet"	0

Fig. 6. Geomorphological context of Cachinales site, indicating the precise position of the studied outcrop with respect to the coastline (black rectangle), calibrated by Differential GPS measurements (see location in Fig. 2).
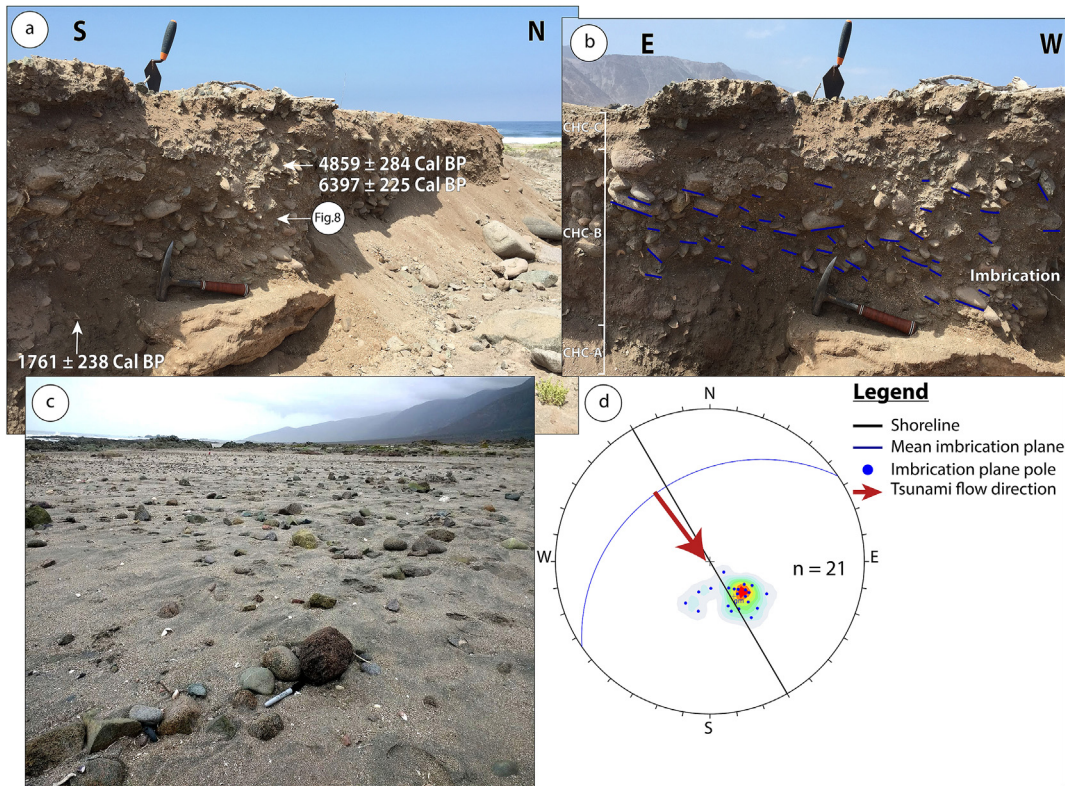
Fig. 7. Detailed geological observations of inferred paleotsunami deposit from the Cachinales site. (a) Natural outcrop, which shows an distinctive layer with well-rounded landward-imbricated clasts, overlain and underlain by alluvium. (b) Detail of the distinctive layer interpreted as a paleotsunami deposit, exhibiting landward-imbricated clasts. (c) Rounded clasts located in the upper tidal and supralittoral environments of the adjacent modern beach. (d) Southeasterly direction of deposition inferred from imbrication measurements.
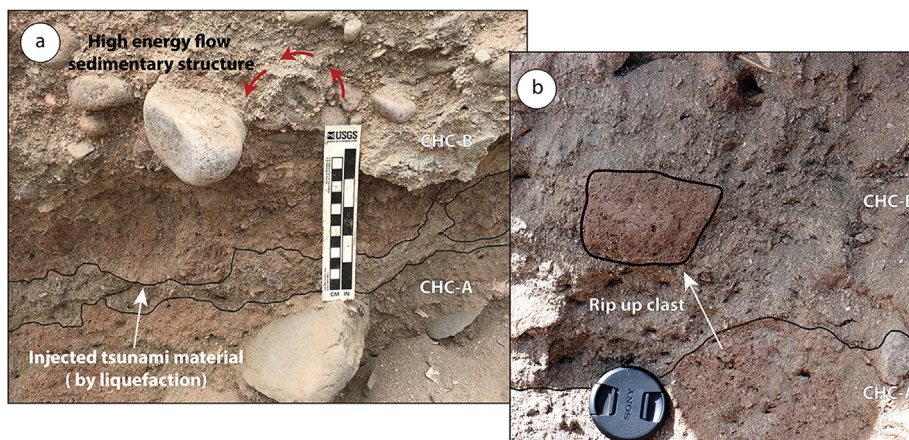
Fig. 8. Detailed observations of sedimentary structures at the base of the inferred paleotsunami layer at the Cachinales site. (a) Rotated shell hash (red arrows) interpreted as a high-energy sedimentary structure close to the erosive basal contact of the paleotsunami deposit, and downward injected material within the underlying deposit most probably associated with liquefaction. (b) Detail of a rip-up clast, taken by a high-energy flow from the underlying deposit, embedded within the basal portion of the paleotsunami layer. (For interpretation of the references to color in this figure legend, the reader is referred to the Web version of this article.)

Radiocarbon results obtained from shells in the upper part of the basal layer (CCH-A) and within the middle layer (CCH-B) gave ages of 1761 ± 238 cal years BP (189 ± 238 CE) and $6397 \pm 225 - 4859 \pm 284$ cal years BP, respectively (Fig. 7a and Table 1). As deposit CCH-B overlies the layer CCH-A (Fig. 7), we interpret the date from the top of the latter, i.e. 1761 ± 238 cal years BP as a maximum age for the former deposit, which most likely reworked mid-Holocene littoral sediments.

3.2.2. Los Bronces trench

At the Los Bronces site we excavated two trenches and provide a detailed description of one of them. The 1.9 m deep trench was located 8 m a.s.l. and 120 m inland (Fig. 9). A stratigraphic analysis of the trench profile revealed two distinctive coarse sand and gravel deposits (TLB-B and TLB-D; Fig. 10), both of them characterized by sharp erosional basal contacts and fining landward (Fig. 10).

At the base of the trench was a layer comprising well-rounded gravel and boulder clasts embedded within sandy matrix with abundant carbonate shell fragments and well-preserved mollusk shells (TLB-A; Fig. 10). This is interpreted as a marine littoral facies. The first distinctive coarse sand and gravel layer (TLB-B) is located 70–90 cm below the ground surface and directly overlies the basal gravel-boulder deposit (Fig. 10). The other distinctive layer (TLB-D) is located 23–45 cm deep and overlies a brownish deposit (Fig. 10) comprised of predominantly well-sorted fine sand of subangular and rounded clasts, with incipient parallel and cross lamination (TLB-C; Fig. 10). We interpret this last deposit as the result of local alluvial reworking of aeolian and littoral sediments. Both of the distinctive layers (TLB-B and D) are characterized by inverse-normal grain size gradation (Fig. 11). In particular, the sandy and fine matrix of TLB-B exhibits a similar grain size distribution to that of the basal littoral deposit (TLB-A; Fig. 10). Layer TLB-D on the other hand has a mixed grain size distribution between those of the littoral sediments and of the alluvially reworked material (TLB-C) directly underlying it (Fig. 10). Elemental analyses show a relative increase in Ca and Fe-content as well as in Sr and Ti within the two distinctive layers (Fig. 1, Appendix A). Both of these distinctive layers (TLB-B and D) also exhibit a relative increase in littoral shell species including large mollusk fauna (*Scurria parasitica, Tegula* sp.) and small gastropods (*Littorina (Austrolittorina) araucana, Eatoniella (Eatoniella) latina, Turritella singularia* and *Aeopus Aliciae*) all of which are indicative of an intertidal environment (Guzmán et al., 1998). There were up to 18 and 7 times more small gastropod shells in TLB-B and TLB-D respectively, than within other units in the profile (Fig. 11). At the base of both distinctive layers (TLB-B and D) we observed flame-like structures indicative of a seaward flow direction. Based upon the marked marine nature of these deposits, and the high-energy nature of their deposition coupled with seaward flame-like structures, we interpret these two peculiar layers as most likely being the result of deposition during tsunami backwash.

The overlaying layer (TLB-E) is comprised of angular and sub-rounded lithic clasts in an angular and subangular medium sandy matrix with poorly defined parallel laminations. We interpret this layer as most likely deposited by local alluvial reworking of aeolian and littoral sediments (Fig. 10). The uppermost layer (TLB-F) is a soil affected by subaerial and pedogenetic processes (Fig. 10).

Radiocarbon results from shells in the lowermost marine littoral deposit produced an age of 4086 ± 283 cal years BP. Charcoal material taken from a thin occupational level directly underlying the lower distinctive layer (TLB-B) yielded a maximum age of 4326 ± 86 cal years BP, while shell samples taken from within this layer were dated to 4048 ± 20 and 3990 ± 186 cal years BP. These last results are consistent with a single date of 4063 ± 286 cal years BP obtained from charcoal material taken from an occupational level directly overlying this same distinctive layer, providing a minimum age for its deposition (Fig. 10).

A single radiocarbon result from a charcoal sample taken at the base of the upper distinctive layer yielded an age of 4362 ± 75 cal years BP, which is slightly older than the ages of 3975 ± 284 and 3963 ± 282 cal years BP obtained from shell samples taken from the underlying deposit (TLB-C; Fig. 10). We interpret the later as most probably due to an "old wood effect" previously reported from this hyperarid region (Ortlieb et al., 2011). Two shell samples taken from within the upper distinctive deposit (TLB-D), gave results of 1498 ± 217 cal years BP and 1087 ± 199 cal years BP. We interpret this last date (863 ± 199 CE; see Table 1) as a maximum age for the deposition of this layer (Fig. 10).

3.2.3. Hornos de Cal trench

Hornos de Cal is a mid-Holocene archaeological shell midden located 10–11 m a.s.l. and 100 m from the coast (Fig. 12). Two trenches were studied and we describe one in detail below (Fig. 13). The 1.1 m deep trench showed five units (HC-B to F) overlying marine littoral deposits at the base (HC-A). A distinctive layer (HC-
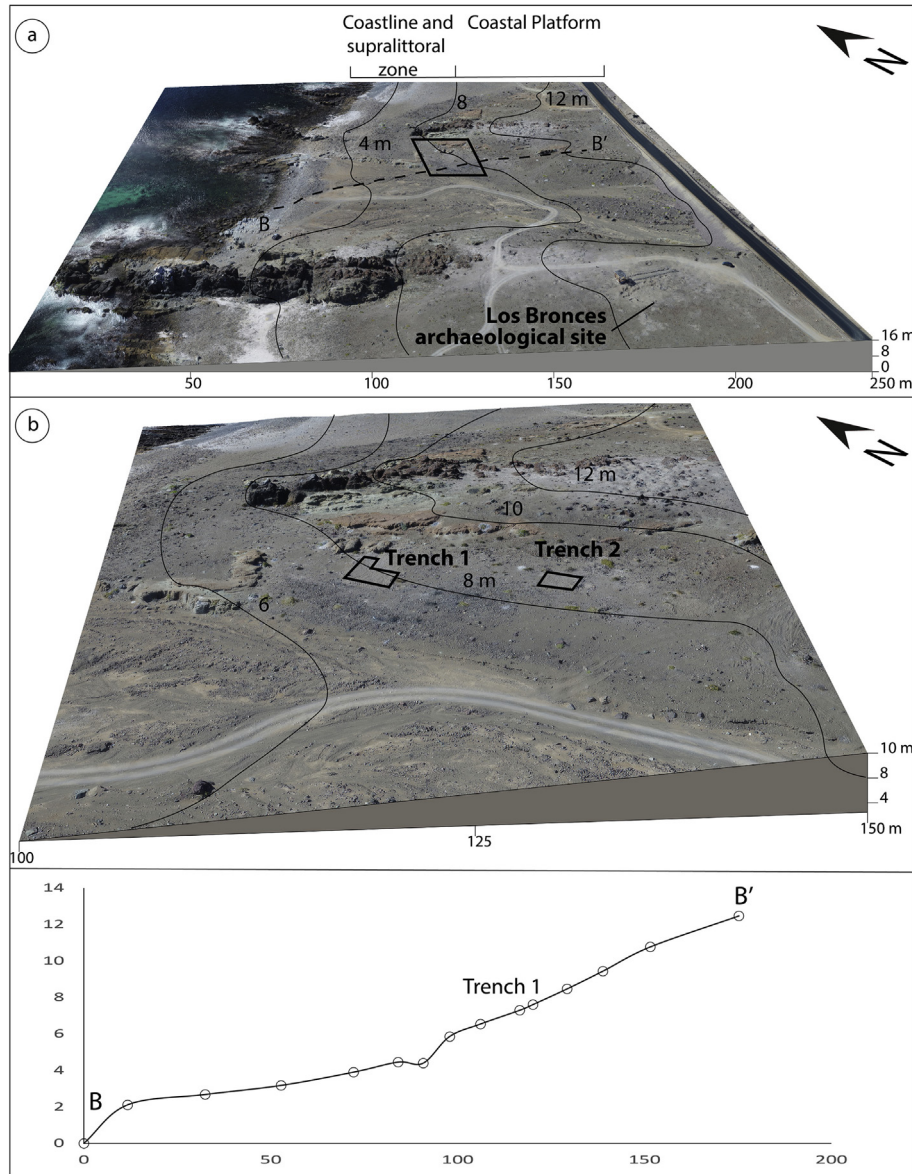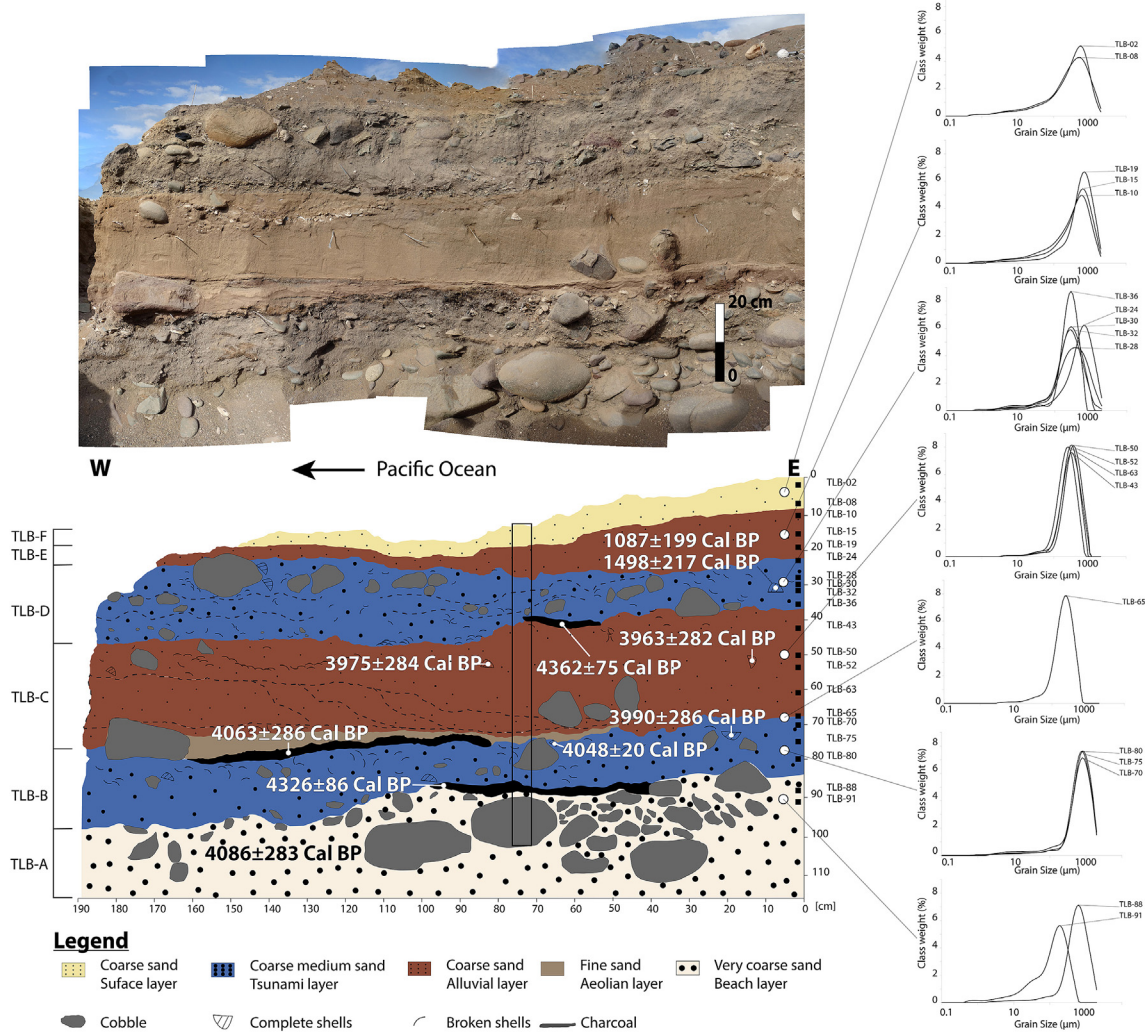
Fig. 9. Geomorphological context of Los Bronces site, indicating the precise position of the studied trenches with respect to the coastline (black rectangle), calibrated by Differential GPS measurements (see location in Fig. 2).

D) exhibits a sharp erosional basal contact and different characteristics with respect to the other geological and archaeological units in the trench (Fig. 13). This is a 15–20 cm thick landward thinning layer. Sedimentological and archaeological analyses revealed that this distinctive layer (HC-D) contains shell fragments, reworked archaeological remains, lithic clasts and minerals chaotically distributed within a fine sandy and organic-archaeological matrix. Much of this material has been sourced from the underlying well-stratified shell midden deposits, and indicates initial erosion and subsequent deposition by high-energy flows (Fig. 13). Sieve grain size analyses indicates a relative decrease in the mean grain size and sorting of particles in this layer with respect to the underlying archaeological deposits (Fig. 14). Laser grain size analyses showed similar grain size distribution of the sandy and fine sedimentary matrix of the distinctive layer (HC-C), with respect to the underlying archaeological strata (HC-B), with a possible contribution of littoral sediments as well (HC-A; Fig. 13). From this distinctive deposit (HC-C), we identified rocky intertidal mollusk

fragments such as *Chitonidae. Scurria parasítica and Tegula* sp., together with small gastropod shells (*Eatoniella (Eatoniella) latina. Turrutella singulata)*, and a sharp decrease in the content of archaeological material with respect to the adjacent strata (Fig. 15). At its basal contact we observed flame-like structures oriented seaward (Fig. 15). Based on these findings we infer that this deposit represents a high-energy seaward flow most probably laid down during tsunami backwash.

Archaeological strata (HC-C and HC-E) are characterized by different sub-units with high organic content such as fish bones and shells, with occupational surfaces enriched in charcoal fragments associated with anthropic hearths. The top gray layer (HC-F) is comprised of a mix of sediments associated with reworking by subaerial processes (Fig. 13).

Radiocarbon data from a single charcoal sample taken at the base of the distinctive layer (HC-D) gave a maximum age of 4491 ± 27 cal years BP. Samples taken from within this deposit yielded radiocarbon dates of 5921 ± 246 and 6339 ± 60 cal years BP,

Fig. 10. Geological mapping of the trench profile at Los Bronces site, showing interpreted paleotsunami deposits (shaded in blue). Results from laser grain size analyses from the sandy and fine matrix are also shown. (For interpretation of the references to color in this figure legend, the reader is referred to the Web version of this article.)
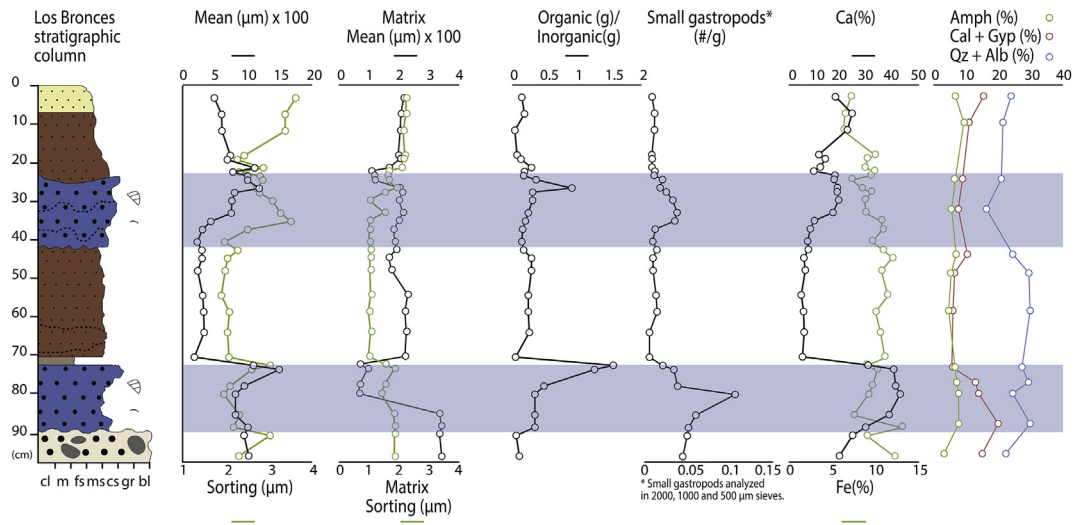
Fig. 11. Results from sieve and laser grain size analyses, stereoscopic observations, geochemical and mineralogical analyses from Los Bronces site (see legend in Fig.10).
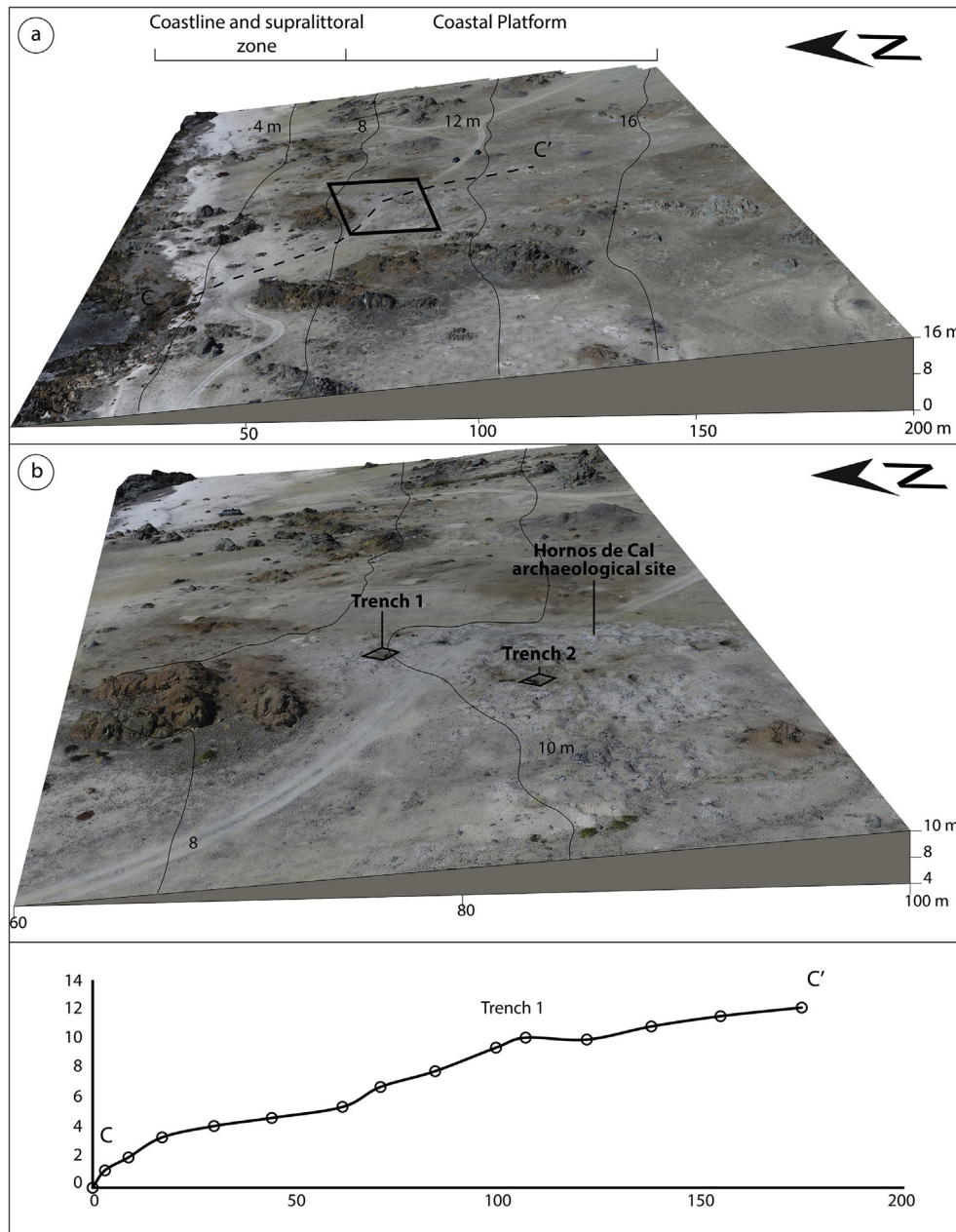
Fig. 12. Geomorphological context of Hornos de Cal site, indicating the precise position of the studied trenches with respect to the coastline (black rectangle), calibrated by Differential GPS measurements (see location in Fig. 2).

most likely indicative of reworking of the underlying archaeological material. A radiocarbon result from charcoals directly overlying the distinctive layer provided a minimum age for it deposition as 4279 ± 129 cal years BP.

4. Discussion

4.1. Identifying tsunami deposits in the hyperarid coastal Atacama Desert

Using multiproxy analyses we have interpreted several distinctive layers as potential Holocene tsunami deposits (CCH-B, TLB-B, TLB-D and HC-D), preserved in the stratigraphic record of Cachinales, Los Bronces and Hornos de Cal sites in the Taltal-Paposo area (Fig. 2).

As previously mentioned, there are several factors that inhibit the preservation of tsunami deposits in this region. Taltal is located at the southern edge of the hyperarid coastal Atacama Desert, where the mean total annual rainfall reaches 15–20 mm, diminishing to almost zero farther north, with 4 mm/year at 23.5°S and less than 1 mm/year at 20.2°S. Precipitation can be almost absent for several years or even decades along these coasts and is only interrupted by sporadic torrential rainfall events during moderate to strong El Niño Southern Oscillation (ENSO) episodes, which can generate debris flows and flooding (Vargas et al., 2000, 2006). Coastal vegetation is limited due to the scarce humidity and lack of perennial rivers (Rundel et al., 1991; Houston, 2006), with small springs fed occasionally by sporadic coastal rains (Herrera and Custodio, 2014). In addition to the dominantly rocky coastline, these conditions serve to prevent the formation of coastal
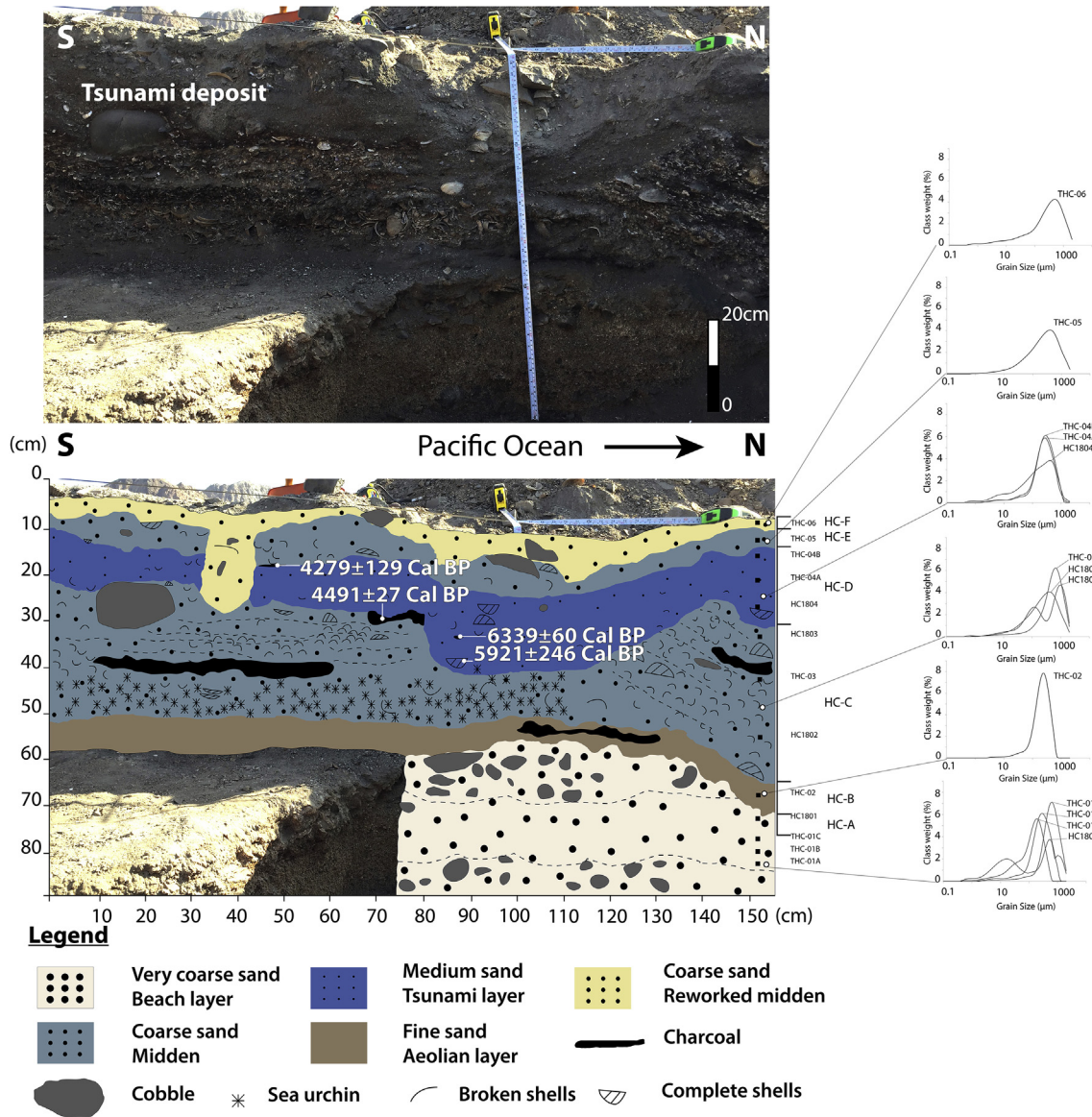
Fig. 13. Geological mapping of the trench at Hornos de Cal site showing the inferred paleotsunami deposit. Results from laser grain size analyses of the sandy/fine matrix are also shown.

wetlands. Furthermore, coastal uplift during the late Quaternary as shown by conspicuous uplifted marine littoral facies at the Los Bronces and Hornos de Cal sites (Figs. 10 and 13), contributes to the suppression of accommodation space onshore. As such, deposits laid down by even the largest tsunamis can easily be eroded or reworked by sporadic debris flows like those in 2015 (Bozkurt et al., 2016), by dominant southwesterly winds, or by storms which can affect the coast along central and northern Chile (Carvajal et al., 2017). On the other hand, preservation can occur in archaeological strata from sheltered coastal occupation sites within the Taltal-Paposo region (Salazar et al., 2015, 2018). At Cachinales, Los Bronces and Hornos de Cal, the candidates for possible tsunami deposits are located between 8 and 11 m a.s.l., well above the influence of tidal variations in the region and sufficiently far inland that they have not been affected by large storm events (Figs. 3—5).

The interpreted tsunami deposit at Cachinales (CCH-B; Fig. 7), is characterized by a medium sandy matrix containing rounded pebbles with conspicuous landward clast imbrication. The massive character of this poorly sorted deposit suggests that it was generated by a hyperconcentrated flow that took sediments from the adjacent beach and transported them inland (Fig. 7). A basal erosional contact, landward thinning, rip-up clasts, shell-hash surrounding some large clasts, liquefaction structures, and dikes of material injected from the upper layer into the lower deposit are all features typically described from tsunami deposits (Le-Roux and Vargas, 2005; Goff et al., 2012). These provide evidence for the occurrence of high velocities and the development of turbulence probably at the leading edge of the flow followed by a hyper-concentrated component that resulted in a characteristically massive deposition similar to that proposed for Neogene paleo-tsunami deposits along the coastal Atacama Desert (Le Roux and Vargas, 2005). The inferred paleotsunami deposit lies between two conspicuous strata characterized by poor sorting and angular clasts, which are chaotically embedded within a sandy and fine matrix, associated with the occurrence of debris flows resulting from heavy rainfalls, most possibly reflecting the influence of El Niño episodes during the mid to late Holocene in the region (Vargas et al., 2006).

Fig. 14. Results from sieve and laser grain size analyses, stereoscopic observations, geochemical and mineralogical analyses from Hornos de Cal site (see legend in Fig.13).
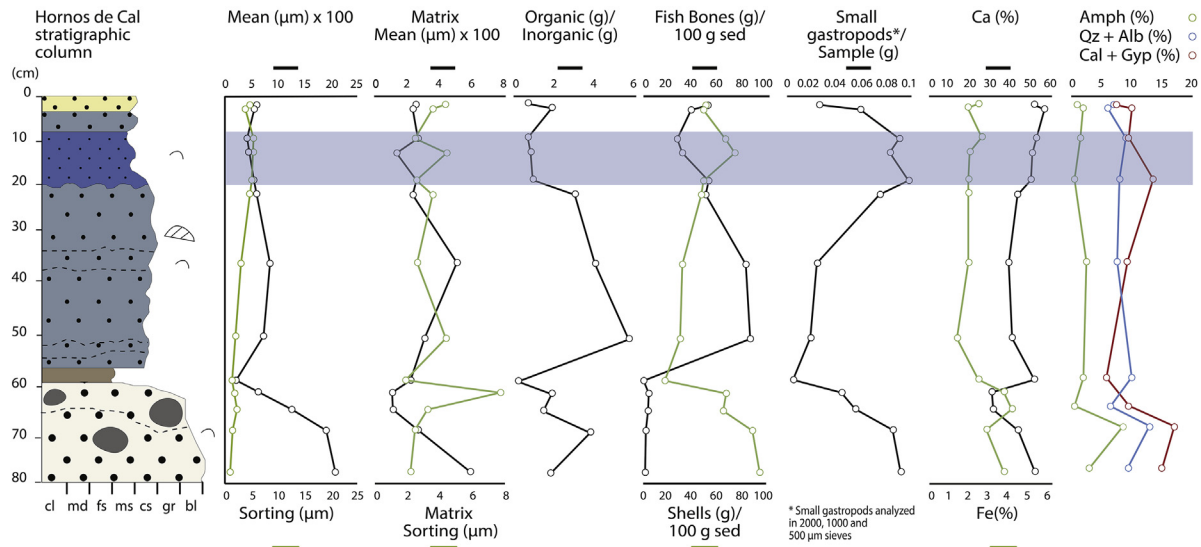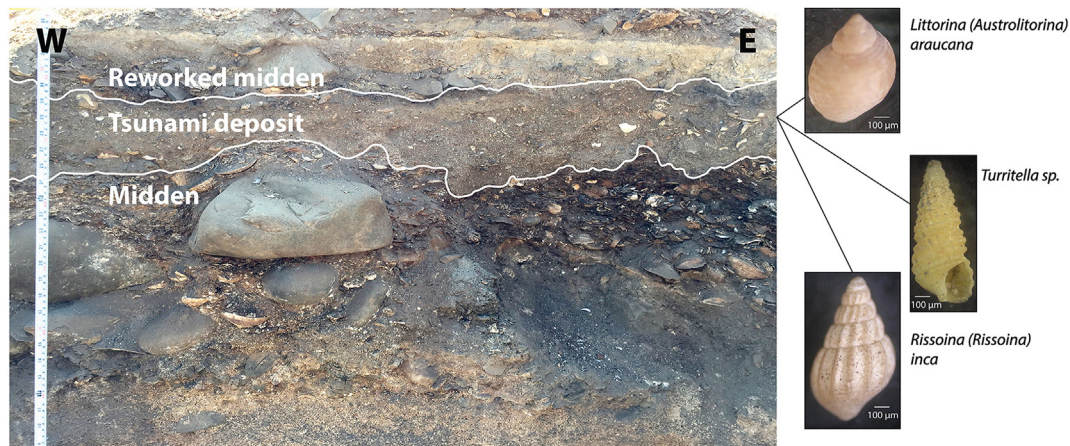

Fig. 15. Hornos de Cal site: Detail of inferred paleotsunami deposit exhibiting erosional basal contact and enrichment in small gastropods. The layer is interbedded between archaeological strata.

At Los Bronces, the two candidate paleotsunami deposits (TLB-B and D) can be differentiated from the underlying and overlying strata. At the base of the trench we observed a layer of well-sorted coarse sediments (pebbles and sand; TLB-A), which we interpret as littoral deposits most likely corresponding to intertidal or beach berm sedimentary facies (Figs. 10 and 11). The alluvial deposits in this trench (TLB-C and E) are markedly different from these marine littoral sediments (TLB-A). Their terrestrial origin is indicated by previously described textural and compositional characteristics, including a relative (to the inferred paleotsunami deposits) decrease in Ca and Fe content. Increases in these elements are normally interpreted as being associated with increases in carbonates and salt water introduced by tsunami inundation (Goff et al., 2012). The trenched section also contains a layer of very well sorted highly rounded spheroidal clasts, which are embedded within a cross-bedded fine sandy matrix (TLB-C) that we interpret as a product of local reworking of aeolian sediments (Nichols, 2009; Flores-Aqueveque et al., 2010).

The two medium sand deposits with gravel clasts that we interpret as paleotsunami deposits (TLB- B and D) exhibit sharp erosional basal contacts, seaward flame structures, inverse-normal grading and landward thinning (Figs. 10 and 11). Normal grading has been described from tsunamis deposits and is interpreted as being the result of decreasing velocity as the wave moves inland producing the settlement of the larger suspended sediment first followed by finer sediment (Goff et al., 2001; Morton et al., 2007; Nichol et al., 2007). However, inverse grading can also occur when there are fine, heavier, sediments at the base of the tsunami flow that can deposit faster than coarser but lighter material above (Morton et al., 2008; Moore et al., 2011; Jaffe et al., 2012). The sharp basal erosional contact and seaward flame structures observed at the base of the deposits (TLB-B and D), suggest that there were high velocity seaward flows most probably associated with paleo-tsunami backwash. Backwash flows can produce strong currents concentrating dense sediment-water mixtures in channels and depressions which initially behave as Bingham fluids dominated by frictional grain interactions and shearing, leading to the formation of shear carpets by kinematic sieving, squeezing and dispersive pressure causing inverse grading (Bagnold, 1954; Middleton, 1967; Le Roux, 2003; Le Roux and Vargas, 2005). These strong backwash currents move as hyperconcentrated flows capable of bringing sediments from the inundated land seaward, including the erosion

of previously deposited paleotsunami layers. The fluidization ahead of these flows forms channels and erosional structures in which concentrated density flows can deposit multiple graded sediments (Dawson, 1994; Schulte et al., 2011; Slootman et al., 2018).

The relative decrease in sorting of the two inferred paleotsunami deposits at Los Bronces relative to the adjacent layers can be interpreted as the result of a mixture of marine and terrestrial sediments being entrained in the dense tsunami backwash flows. Both fine and coarse particles are more rounded in these layers than in the alluvial deposits, supporting the inference of the inclusion of sea-rounded sediments. A distinguishing feature common to the two layers is the presence of both intact and broken marine shells some of them showing a seaward imbrication, consistently with tsunami backwash. Geochemical data also supports the inference of a marine source for these layers (TLB-B and D). There are relative increases in Ca and Sr content associated with carbonates constituting marine shells and microfossils, as well as a slight increase in Ti and Fe content possibly reflecting changes in the concentration of heavy minerals by high-energy depositional processes like reported from tsunami deposits in other environments (Goff et al., 2004; Nichol et al., 2007). Finally, the marine faunal assemblage contained in these deposits reflects an intertidal rocky environment, especially in the case of the small gastropod species that we identified (Fig. 15). These species are not found abundantly in archaeological shell middens in the region, and never occur without a dominant large gastropod shell assemblage (Olguín et al., 2015). This supports the interpretation that the two distinctive layers enriched in small gastropod species were most likely produced naturally by high-energy tsunami backwash rather than by human activity.

At Hornos de Cal, the distinctive layer that we interpret as being the result of tsunami backwash deposition (HC-D) exhibits similar characteristics those in the Los Bronces trench. This layer is comprised of gravel clasts chaotically embedded within a medium sand and fine matrix of reworked archaeological material, separating two occupational strata (Figs. 10 and 11). This layer thins inland (as observed in the landward trench), exhibits inverse grading, and possesses a sharp erosional basal contact with seaward flame structures. As previously discussed, these characteristics can be associated with deposition during tsunami backwash by a hyperconcentrated flow (Le Roux and Vargas, 2005). As noted for the Los Bronces trench, this interpretation is also supported by the observation of shells imbricated seaward and the relative increase in small gastropod shells. Both are consistent with natural deposition by high-energy seaward flow rather than human activity. Organic material within the interpreted paleotsunami deposit (HC-D) comprises a mix of both edible and inedible fauna most likely resulting from the reworking of the underlying shell midden during inundation. Indeed, the introduction of inedible intact shells of small gastropod species (Fig. 15), together with the observed decrease in fish bones-content in the tsunami deposit supports this reworking hypothesis (Fig. 14). In contrast to the in situ archaeological deposits (HC-C and E) and tsunami layer (HC-D), the surface layer (HC-F) in Hornos de Cal site shows clear evidence of erosion and reworking of material by modern human looting which has disrupted previous strata at several areas of the site (Fig. 13).

4.2. Chronological determination of Holocene paleotsunami episodes

Geochronological determinations based on radiocarbon dates from Cachinales, Los Bronces and Hornos de Cal point to the occurrence of at least two –possibly three-large tsunamis that affected the Taltal-Paposo coastal region during the mid and late Holocene.

At Los Bronces, radiocarbon results from reworked shells from the lower interpreted tsunami deposit yielded a maximum calibrated age of 3990 ± 286 cal years BP. Two additional shells taken from this same deposit gave consistent radiocarbon dates of 4326 ± 86 and 4048 ± 86 cal years BP. The minimum age for this event is provided by a date obtained from a charcoal level directly overlying the tsunami deposit, which gave value of 4063 ± 286 cal years BP. Therefore, the first Holocene paleotsunami inferred from the Los Bronces trench can be well constrained to ~4000 cal yrs BP. This tsunami deposit is laid down directly on littoral intertidal or beach berm facies dated to 4086 ± 286 cal years BP.

Holocene sea level variations are poorly constrained along this active tectonic margin. From a global perspective, eustatic variations based on inverted global observations, suggest that the sea level stabilized between 6.7 and 4.2 ka BP, following the deglaciation, with no significant oscillations in ice volume-deduced global-mean sea level of amplitude exceeding 15–20 cm, until 100–150 years ago when it begun to rise again, with less than 1 m as a total in this last period (Lambeck et al., 2014). Relative sea level changes have been discussed from uplifted wetland records in central Chile, proposing a mid Holocene high sea level stand at about +1–3 m with respect to its modern position, which occurred between 7 and 5 ka BP, followed by a gradual fall until present (Dura et al., 2016). It is expectable that this maximum mid Holocene relative sea level would has been lower at lower latitudes of South America (Khan et al., 2015).

Thus, since the littoral deposits at the basal section of Los Bronces trench are at an altitude of +7 m a.s.l. It is possible to infer an uplift rate in the order of 1–1.5 m/ka over the past ~4 ka (allowing for a maximum relative sea level riser of +1–3 m a.s.l. During the mid Holocene; Lambeck et al., 2014; Khan et al., 2015; Dura et al., 2016). This is similar to those calculated from uplifted late Pleistocene and Holocene littoral deposits in the Mejillones peninsula and neighboring coasts (González-Alfaro et al., 2018).

At Hornos de Cal, the maximum age of the interpreted paleotsunami deposit is constrained by an underlying anthropic level, which gave a radiocarbon date of 4491 ± 27 cal years BP. Two additional results from reworked charcoal and shell from this deposit gave values of 6339 ± 60 and 5921 ± 246 cal years BP. These maximum ages are close to those obtained from the lower tsunami deposit at Los Bronces site and probably reflect the same paleotsunami event that most likely occurred ~4000 cal yrs BP, as also supported by the minimum age of 4279 ± 129 cal years BP obtained from Hornos de Cal site. The direct contact relationship together with similar age results obtained from the lower paleotsunami deposit at Los Bronces and from the underlying littoral deposits at the base of the same trench, suggests that this tsunami episode would have been preceded by a sudden coastal uplift that fossilized the previously formed beach berm, pointing to a regional tectonic source for this event. This is most likely related to a large earthquake on the Nazca-South America interplate contact adjacent to the Taltal region which uplifted the coast as observed in the case of the moderate 1995 CE Antofagasta and 2007 CE Tocopilla earthquakes (Ortlieb et al., 1996; González-Alfaro et al., 2018), whose epicenters were situated underneath the southern and northern Mejillones peninsula, respectively. Furthermore, uplifted littoral deposits located up to +7 m a.s.l. and dated as 3728 ± 105–4299 ± 110 cal years BP at Playa Grande, which is located on the northern edge of the Mejillones peninsula (González-Alfaro et al., 2018), tend to support the occurrence of a large tsunamigenic megathrust event close to ~4000 cal yrs BP in the Taltal-Mejillones region (Fig. 1).

At Los Bronces, the trench exhibits an upper layer interpreted as

a paleotsunami deposit that is constrained by radiocarbon dates of 1498 ± 217 cal years BP and 1087 ± 199 cal years BP from reworked shells within it, suggesting the last as a maximum age for the deposition of this tsunami layer (863 ± 199 CE; Table 1). At Cachinales, the maximum age of the inferred paleotsunami deposit is given by a radiocarbon date from shells in reworked material directly underlying this deposit. These yielded a date of 189 ± 238 CE (1761 ± 238 cal years BP; Table 1). Considering that these are maximum ages obtained from reworked material within sediment strata in both sites, it is possible to infer that these deposits could represent a single large tsunami episode that occurred after ~863 CE. However, the age of this event is poorly constrained and it is not possible to discard that the inferred paleotsunami deposit found at Cachinales could represents a previous event occurred closely after ~189 CE. Additional dating is needed to give a more precise timing, as well as to elucidate if these deposits could represent either a single event or two distinct but chronologically close tsunami episodes. Despite this though, the geological evidence tends to suggest that it strongly impacted the coastal area of Taltal-Paposo, probably as significantly as the earlier, well constrained ~4000 cal yrs BP event.

The observation of large boulders, some of them exhibiting a landward imbrication at Matancillas beach just to the north of Cachinales (Figs. 2 and 16), can be taken as possible additional evidence for the occurrence of large Holocene tsunamis along this coast, although more research is needed to determine the dating and depositional origins of these blocks.

4.3. Implications for tsunami hazard assessment in the area

From the review of articles, books, reports and newspapers, we have reanalyzed the impact of the historical tsunamis of 1877 CE and 1922 CE in the Taltal coastal region (Table 2). The few available historical records confirm that the 1877 CE megathrust generated a tsunami that significantly affected the region, even though no detailed information about the extent of inundation in Taltal city has been found (Fig. 17). However, the tsunami inundation map available for this city (CITSU, SHOA, 2012), indicates that the 1877 CE event would have generated maximum run-ups in the order of +7 m a.s.l., with an inundation that reached around 170 m inland from the coastline. Such an inundation is consistent with the magnitude of M_w 8.9–8.7 inferred for the size of this major megathrust (Kausel, 1986; Comte and Pardo, 1991; Ruiz and Madariaga, 2018), which caused a major tsunami with an estimated magnitude of 9.0 (Abe, 1979; Ruiz and Madariaga, 2018).

For the 1922 CE tsunami, which was generated by a seismic rupture localized to the south of the study area (Fig. 1), there is more detailed historical information from which we can determine

Fig. 16. Large blocks in Matancillas beach, located to the north of Cachinales site, which probably reflect tsunami deposition (view towards the south).

that the flooding caused by this event reached Esmeralda Street about 5 m a.s.l. and 50 m inland from the coastline in Taltal city. The differences in run-up and inundation between these two events are most likely related to the nature and size of the earthquakes, the amount of deformation of the sea floor in the near-trench zone, and the direction of tsunami wave inundation from these sources. The epicenter of the 1922 CE earthquake was initially located underneath the continent, but subsequent research proposed a M_w ~8.5 for its size and a tsunami magnitude of 8.7, encompassing an area close to the trench (Abe, 1979; Ruiz and Madariaga, 2018).

The reanalysis of the historical data from several localities along coastal northern Chile reveals a rapid decrease in tsunami run-up estimations northwards from the 1922 CE rupture area, with run-up values of around +10–12 m close to the source. Similarly, run-up estimations decrease southwards from the rupture area of the 1877 CE giant megathrust, with initial values of around +20–22 m along the coast located close to the source (Fig. 17). These observations indicate that the seismic ruptures of these last two megathrusts did not involve the subduction interface encompassing the Taltal region, thus, confirming that there is significant slip deficit along this seismic gap region like previously proposed from geodetic survey (Métois et al., 2016).

The geo-archaeological record reported here indicates the occurrence of significantly larger Holocene events than have been recorded in historical times in the Taltal region. The older paleotsunami which occurred close to ~4000 cal yrs BP reached minimum tsunami run-ups of +7 m and +10 m a.s.l. at Los Bronces and Hornos de Cal, with minimum inundations of 120 m and 100 m from the coastline, respectively (Fig. 17). In the case of the younger paleotsunamis which occurred after ~863 CE, and possibly after ~863 CE, the deposits observed at Los Bronces and Cachinales suggest minimum run-ups of +8–9 m, with a minimum inundation of 120 m from the coastline at both sites. Thus, for all of the Holocene paleotsunami events it is possible to infer that the respective inundations were larger than those of the 1877 CE and 1922 CE tsunamis in the area.

The 1877 CE earthquake generated a trans-Pacific tsunami for which significant run-ups and deposits have recently been reported from the east coast of New Zealand (Donnelly et al., 2017) and Japan (Tsuji, 2013). This is consistent with the expected propagation of the tsunami's main energy across the Pacific Ocean from the source areas associated with the 1877 CE and 1922 CE earthquakes (Goff et al., 2010). A review of paleotsunami records in the south western Pacific region reveals that there are six reported sites along the east coast of New Zealand that have been linked to a potential earthquake along the northern Chilean coast around 1500 years ago (New Zealand Palaeotsunami Database, 2018), near-contemporaneously with the younger events inferred in the Taltal area. There is more geological evidence for an earlier paleotsunami that occurred around 4000 years ago in the SW Pacific region. Sites have been reported from the east coast of New Zealand (up to seven sites), in SE Australia (two), Vanuatu (two) and Samoa (one) (Switzer et al., 2005; Clark et al., 2011; Goff et al., 2011; Williams et al., 2011; New Zealand Palaeotsunami Database, 2018). Most recently, work from Chatham Island in New Zealand's most easterly archipelago reported a fine sediment and boulder deposit some 3 m a.s.l. That could be traced up to 1100 m inland (Goff et al., 2018). This was dated to 3500–4500 cal yrs BP, and numerical modelling associated this event with a distant tsunami generated by a large megathrust along the northern Chile seismic gap (Goff et al., 2018). All of the above data provide supporting evidence for the occurrence of large Holocene tsunamis whose most probably source was the subduction interplate contact along the major northern Chile seismic gap encompassing the Taltal-Paposo region.
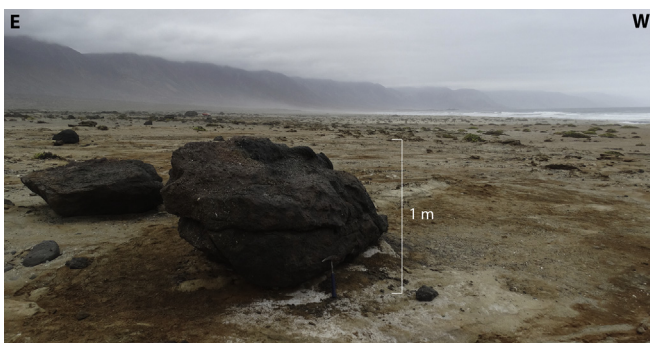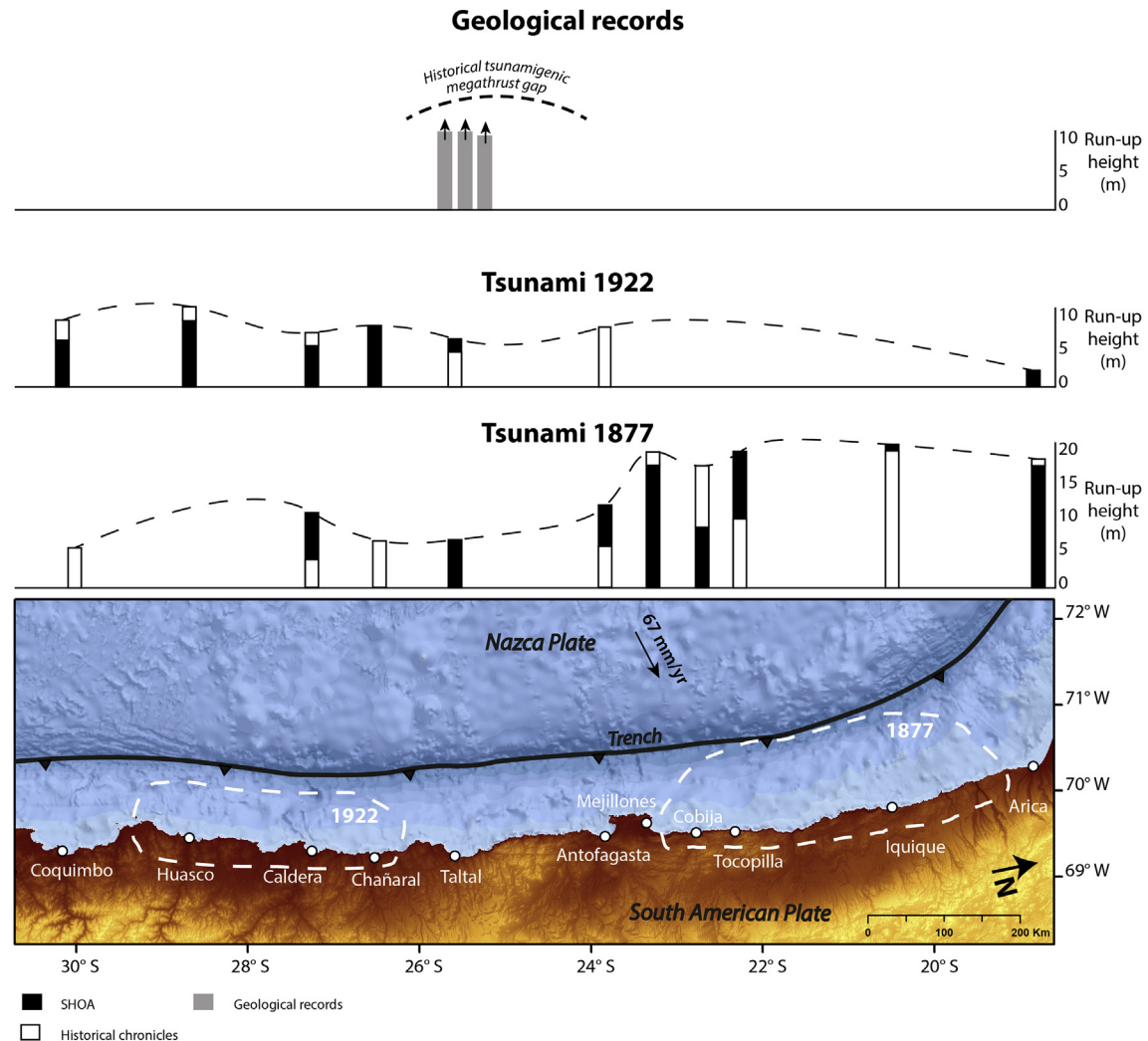
Fig. 17. Historical run-ups for the 1877 CE and 1922 CE tsunamis in some of the main localities along the northern Chile coasts, as revealed by the review of chronicles (Table 2) and official reports (CITSU, SHOA).

5. Conclusions

The ability to identify tsunami deposits along the hyperarid coastal Atacama Desert adjacent to the subduction contact margin of the Nazca and South American plates, is challenged by several factors. These include the scarcity of appropriate depositional environments, limited or even suppression of accommodation space for tsunami deposition and preservation, and the sporadic occurrence of debris flows, storms or even wind deflation that can erode any possible sediments. Despite this, archaeological sites located all along these coasts offer an opportunity for the identification of tsunami deposits interbedded between well preserved anthropogenic strata.

Using a multiproxy approach that included geomorphological, stratigraphic, sedimentological, geochemical, paleontological and archaeological analyses, we identified paleotsunami deposits at Cachinales, Los Bronces and Hornos de Cal in the Taltal-Paposo coastal region. These deposits possess numerous characteristics indicative of tsunami deposition such as basal erosional contacts, flame structures, inverse grading, mixed well rounded and subangular gravels embedded in a sandy and fine matrix, high concentrations of rocky intertidal shellfish species and other distinctive compositional characteristics.

Geochronological determinations based on calibrated radiocarbon dates from littoral marine shells along these hyperarid coasts are challenged by the possibility of dating reworked material embedded in paleotsunami deposits, and the presence of charcoal from old wood fragments. Despite this, radiocarbon results from shells and charcoals suggest that paleotsunami deposits identified in this work most probably reflect at least two large tsunamis that occurred during the mid and late Holocene. The age of the earlier Holocene paleotsunami is well constrained to ~4000 cal years BP by radiocarbon results from shell and charcoal samples taken from within, as well as from the layers directly underlying or overlying the corresponding deposits at Hornos de Cal and Los Bronces. The second inferred paleotsunami is constrained by calibrated radiocarbon results from samples taken within the paleotsunami deposits at Los Bronces and Cachinales and give a maximum age of 863 ± 199 CE. Nonetheless, it is not possible to discard a previous event, which would has occurred closely after 189 ± 238 CE according the available geochronological record from the inferred paleotsunami deposit at Cachinales.

The reanalysis of historical records associated with the most recent large tsunamis in the area caused by the M_w ~8.8 1877 CE and M_w ~8.5 1922 CE events suggests that these were considerably smaller than their paleotsunami counterparts. This emphasizes the

==need for a re-evaluation of the tsunami hazard in this segment of the major northern Chile seismic gap as well for the wider Pacific Ocean basin.== Further research is needed to better understand the tectonic origin as well as the magnitude of the large Holocene paleotsunamis reported here and, importantly, the impact that these events had on early inhabitants along the hyperarid coastal Atacama Desert.

Data availability

The samples data used to generate this article can be found in: https://data.mendeley.com/datasets/jjg6r5btkz/draft?a=ee3a9458-e067-4193-80e2-f946e23b67a7.

Appendix A. Los Bronces trench data

XRF (Results in wt.%)

Sample	Depth (cm)	Si	Al	Ba	Br	Ca	Cl	Cu	Fe	I	K
TLB-3	3	36.516	16.838			17.933		0.152	7.126		4.247
TLB-7	7	30.135	13.491	0.185	0.011	24.293	3.123	0.101	6.482		3.503
TLB-11	11	31.950	14.176			22.521		0.094	6.319		3.757
TLB-17	17	41.039	19.181			11.574		0.237	9.891		3.431
TLB-18	18	39.311	17.449			14.037		0.266	9.033		3.062
TLB-20	20	41.901	18.298			12.104		0.438	8.751		3.309
TLB-21	21	42.766	19.728			9.622		0.573	9.852		3.535
TLB-22	22	36.243	17.282			17.761		0.422	9.395		3.272
TLB-23	23	37.198	16.554			17.436		0.336	7.277		3.127
TLB-25	25	36.674	15.667			18.672		0.550	8.385		3.211
TLB-26	26	35.873	15.648			18.595		0.273	9.495		3.262
TLB-27	27	34.976	15.983			19.179		0.352	8.739		3.426
TLB-31	31	38.022	15.761			17.004		0.180	8.868		3.260
TLB-33	33	42.466	18.316	0.186		9.865		0.137	10.634		3.209
TLB-35	35	45.386	20.046			8.303		0.094	10.807		4.185
TLB-38	38	48.107	20.729			7.247		0.120	9.568		3.586
TLB-40	40	46.806	20.077			7.528		0.249	10.875		3.653
TLB-42	42	46.606	20.410			5.805		0.133	11.907		3.099
TLB-45	45	48.177	21.446			6.353			10.651		3.180
TLB-51	51	47.138	21.760			4.801		0.339	11.373		2.608
TLB-53	53	47.788	21.125			5.691		0.292	9.967		3.210
TLB-55	55	46.806	21.271			5.915		0.328	10.515		2.946
TLB-66	66	46.541	20.843			5.262		0.178	11.032		3.129
TLB-68	68	24.006	10.676			30.482		2.447	8.947		2.190
TLB-69	69	18.389	7.735			40.309		2.605	10.151		1.855
TLB-73	73	20.778	8.492			41.043	4.155	1.339	9.617	0.063	1.952
TLB-79	79	20.535	8.013			42.829	3.800	0.760	9.164	0.107	2.324
TLB-82	82	21.318	7.693		0.016	38.533		0.540	7.466		1.876
TLB-83	83	25.385	10.931			29.530		0.593	12.997		2.285
TLB-89	89	29.715	12.198	0.229		24.527		0.276	8.975		2.438
TLB-90	90	38.447	16.391			19.472		1.105	12.166		3.280

XRF (Results in wt.%)

Sample	Mg	Mn	P	Pb	Rb	S	Sc	Sm	Sr	Ti	V	Y	Zn	Zr
TLB-3	12.094	0.260	3.080		0.028	0.734			0.213	0.683	0.031		0.044	0.021
TLB-7	11.594	0.227	5.443		0.024	0.492			0.252	0.608			0.037	
TLB-11	11.991	0.242	4.775		0.026	0.405	2.766		0.256	0.659	0.028		0.035	
TLB-17	9.813	0.236	3.003		0.025	0.422			0.212	0.828	0.042	0.007	0.060	
TLB-18	10.800	0.233	4.350		0.026	0.309			0.215	0.809	0.031		0.071	
TLB-20	11.071	0.208	2.509		0.021	0.269			0.192	0.831			0.098	
TLB-21	9.950	0.306	2.217		0.021	0.236			0.145	0.868	0.046	0.007	0.128	
TLB-22	9.802	0.225	3.973		0.023	0.338			0.205	0.925	0.029	0.006	0.100	
TLB-23	12.301	0.237	4.081		0.018	0.448			0.212	0.610	0.020		0.078	0.065
TLB-25	8.910	0.322	5.025		0.019	1.516			0.229	0.661	0.022		0.123	0.015
TLB-26	10.083	0.298	3.680		0.024	1.624			0.254	0.709		0.006	0.071	0.104
TLB-27	11.005	0.324	4.185		0.023	0.698			0.285	0.711			0.088	

(continued)

Sample	Mg	Mn	P	Pb	Rb	S	Sc	Sm	Sr	Ti	V	Y	Zn	Zr
TLB-31	10.632	0.323	4.343		0.023	0.394			0.276	0.806	0.036		0.054	0.016
TLB-33	11.092	0.300	1.509		0.022	1.341			0.143	0.691			0.051	0.030
TLB-35	8.316	0.333	1.221		0.025	0.308			0.074	0.802	0.049	0.008	0.043	
TLB-38	8.562	0.252	0.386		0.024	0.362			0.092	0.914		0.007	0.045	
TLB-40	8.807	0.306			0.027	0.437			0.109	1.012	0.043		0.072	
TLB-42	10.190	0.246			0.020	0.516			0.057	0.872	0.041		0.054	0.044
TLB-45	8.454	0.284			0.017	0.193			0.036	1.065	0.055		0.041	0.047
TLB-51	10.193	0.296			0.017	0.378			0.039	0.914	0.051		0.093	0.031
TLB-53	9.921	0.271			0.016	0.517			0.042	0.988	0.055		0.084	0.040
TLB-55	10.359	0.220				0.520			0.035	0.856	0.044		0.096	
TLB-66	11.162	0.301			0.018	0.419			0.040	0.965	0.050		0.060	
TLB-68	9.554	0.295	7.154		0.026	0.498			2.076	1.159	0.041		0.447	
TLB-69	0.000	0.576	7.079		0.027	0.527	6.197		2.680	1.364			0.506	
TLB-73	0.000	1.262	7.357			0.672		0.164	1.537	1.292			0.276	
TLB-79	0.000	1.382	6.976	0.081		0.842			2.027	0.945	0.052		0.161	
TLB-82	9.420	0.956	8.138	0.096	0.018	0.736			2.457	0.591	0.030		0.116	
TLB-83	7.886	0.381	6.598	0.126		1.491			1.142	0.459	0.016		0.143	
TLB-89	9.141	0.269	6.391	0.056	0.025	0.953	2.946		1.192	0.597			0.073	
TLB-90	0.000	0.459	4.951	0.068	0.030	1.719			0.493	1.156	0.052		0.211	

Gastropod counting.

Sample	Depth (cm)	N° gastropods	N° foraminiferous	Sample weight (g)	Individuals per sample (#/g)
TLB-3	3	1		320.09	0.0031
TLB-7	7	2		332.54	0.0060
TLB-11	11	2		343.72	0.0058
TLB-17	17	1		368.86	0.0027
TLB-18	18	1		310.43	0.0032
TLB-20	20	1		344.78	0.0029
TLB-21	21	2		313.58	0.0063
TLB-22	22	2		365.03	0.0054
TLB-23	23	6		392.88	0.0152
TLB-25	25	5	2	398.11	0.0125
TLB-26	26	7		353.79	0.0197
TLB-28	27	8		292.27	0.0273
TLB-31	31	10		309.64	0.0322
TLB-33	33	8		268.89	0.0297
TLB-35	35	2		296.86	0.0067
TLB-38	38	1		254.63	0.0039
TLB-40	40	2		231.52	0.0086
TLB-42	42	1		240.11	0.0041
TLB-45	45	1		235.06	0.0042
TLB-51	51	2		256.45	0.0077
TLB-53	53	2		224.12	0.0089
TLB-55	55	0		231.25	0
TLB-66	66	0		210.18	0
TLB-68	68	5		319.5	0.0156
TLB-69	69	9		314.65	0.0286
TLB-73	73	10		302.46	0.0330
TLB-79	79	33	3	328.73	0.1003
TLB-82	82	16		294.4	0.0543
TLB-83	83	14		305.74	0.0457
TLB-89	89	13		294.57	0.0441
TLB-90	90	11		282.7	0.0389

Sphericity and Roundness

Sample	Depth (cm)	Sphericity	Roundness
TLB-03	3	2.5	1.5
TLB-07	7	4.5	0.5
TLB-11	11	-2.5	1.5
TLB-17	17	4.5	2.5
TLB-18	18	-2.5	0.5
TLB-20	20	-2.5	1.5
TLB-21	21	2.5	1.5
TLB-22	22	-2.5	4.5
TLB-23	23	4.5	3.5
TLB-25	25	2.5	3.5
TLB-26	26	-2.5	3.5
TLB-27	27	4.5	2.5
TLB-31	31	0.5	1.5
TLB-33	33	2.5	0.5
TLB-35	35	4.5	1.5
TLB-38	38	2.5	1.5
TLB-40	40	2.5	1.5
TLB-42	42	4.5	0.5
TLB-45	45	4.5	3.5
TLB-51	51	-2.5	0.5
TLB-53	53	-2.5	0.5
TLB-55	55	2.5	0.5
TLB-66	66	2.5	1.5
TLB-68	68	2.5	5.5
TLB-69	69	-2.5	3.5
TLB-73	73	-2.5	3.5
TLB-79	79	-2.5	2.5
TLB-82	82	-2.5	1.5
TLB-83	83	2.5	2.5
TLB-89	89	-2.5	4.5
TLB-90	90	2.5	3.5

FTIR analysis (wt. %)

Sample	Depth (cm)	Amph	Qz+Alb	Cal+gyp
TLB-3	3	6.8	24.0	15.5
TLB-7	7	9.5	21.5	11.0
TLB-11	11			
TLB-17	17			
TLB-18	18			
TLB-20	20			
TLB-21	21			
TLB-22	22			
TLB-23	23	6.5	21.0	9.0
TLB-25	25			
TLB-26	26			
TLB-28	28	5.5	16.4	7.7
TLB-31	31			
TLB-33	33			
TLB-35	35			
TLB-38	38			
TLB-40	40	7.0	24.5	10.5
TLB-42	42			
TLB-45	45	5.3	29.5	6.5
TLB-51	51			
TLB-55	55	4.7	29.9	6.0
TLB-60	60			
TLB-66	66			
TLB-68	68			
TLB-69	69	6.7	27.4	6.0
TLB-73	73			
TLB-75	75	7.2	29.4	13.0
TLB-80	80	7.8	24.5	14.0
TLB-83	83	7.8	29.9	20.0
TLB-85	85			
TLB-90	90	3.3	22.4	15.1

Organic vs. inorganic material

Sample	Depth (cm)	Organic (%)	Inorganic (%)	Ratio (org/inorg)
TLB-3	3	13	87	0.149
TLB-7	7	16	84	0.190
TLB-11	11	4	96	0.041
TLB-17	17	7	93	0.075
TLB-18	18	12	88	0.136
TLB-20	20	23	77	0.298
TLB-21	21	16	84	0.190
TLB-22	22	15	85	0.176
TLB-23	23	27	73	0.369
TLB-25	25	48	52	0.923
TLB-26	26	24	76	0.315
TLB-28	27	24	76	0.315
TLB-31	31	20	80	0.25
TLB-33	33	17	83	0.204
TLB-35	35	14	86	0.162
TLB-38	38	13	87	0.149
TLB-40	40	15	85	0.176
TLB-42	42	23	77	0.298
TLB-45	45	23	77	0.298
TLB-51	51	20	80	0.25
TLB-53	53	20	80	0.25
TLB-55	55	21	79	0.265
TLB-66	66	5	95	0.052
TLB-68	68	61	39	1.564
TLB-69	69	56	44	1.272
TLB-73	73	33	67	0.492
TLB-79	79	26	74	0.351
TLB-82	82	26	74	0.351
TLB-83	83	26	74	0.351
TLB-89	89	6	94	0.063
TLB-90	90	10	90	0.111

Sedimentological parameters (μm)

Sample	Depth (cm)	Mean	Sorting	Skewness	Kurtosis
TLB-3	3	489.341	3.621	-0.187	1.456
TLB-7	7	601.871	3.375	-0.131	1.363
TLB-11	11	606.903	3.377	-0.165	1.405
TLB-17	17	736.671	2.427	0.031	1.769
TLB-18	18	691.369	2.264	-0.062	1.790
TLB-20	20	1111.568	2.874	0.239	1.151
TLB-21	21	776.359	2.311	0.078	1.594
TLB-22	22	1004.495	2.794	0.150	1.150
TLB-23	23	1002.504	2.860	0.099	1.117
TLB-25	25	1183.499	2.719	0.216	0.931
TLB-26	26	801.544	2.783	0.012	1.214
TLB-28	27	761.416	3.088	-0.006	1.156
TLB-31	31	751.535	3.269	-0.005	0.995
TLB-33	33	435.051	3.513	0.140	1.047
TLB-35	35	305.274	2.507	0.279	0.991
TLB-38	38	224.583	1.974	0.162	1.216
TLB-40	40	297.512	2.279	0.065	1.228
TLB-42	42	300.543	2.041	-0.035	1.035
TLB-45	45	233.439	1.985	0.041	1.089
TLB-51	51	309.058	1.895	-0.066	1.163
TLB-53	53	324.894	2.082	0.017	1.084
TLB-55	55	331.654	2.042	-0.018	0.949
TLB-66	66	180.764	2.072	-0.106	1.454
TLB-68	68	1095.028	3.030	0.055	0.805
TLB-69	69	1492.053	2.604	-0.034	0.650
TLB-73	73	953.370	2.101	0.180	1.188
TLB-79	79	815.298	1.956	0.160	1.260
TLB-82	82	816.624	2.315	0.144	1.324
TLB-83	83	1009.897	2.183	0.200	1.102
TLB-89	89	949.451	3.026	0.102	1.017
TLB-90	90	1020.362	2.302	0.116	0.995

Matrix sedimentological parameters (μm)

Sample	Depth	Mean*100	Sorting
TLB-3	3	2.14	2.23
TLB-7	7	2.04	2.23
TLB-11	11	2.01	2.13
TLB-17	17	1.95	2.18
TLB-18	18	2.01	2.13
TLB-20	20	1.64	2.06
TLB-21	21	1.07	1.63
TLB-22	22	1.16	1.61
TLB-23	23	1.17	1.63
TLB-25	25	1.99	1.92
TLB-26	26	2.08	1.52
TLB-28	28	1.99	1.03
TLB-31	31	2.11	1.51
TLB-33	33	1.98	1.03
TLB-35	35	1.79	1.02
TLB-38	38	1.84	1.02
TLB-40	40	1.88	1.04
TLB-42	42	1.65	1.03
TLB-45	45	1.72	1.03
TLB-51	51	2.27	1.06
TLB-55	55	2.19	1.01
TLB-60	60	2.23	1.06
TLB-66	66	2.19	1.01
TLB-68	68	0.70	1.54
TLB-69	69	0.96	1.85
TLB-73	73	0.70	1.54
TLB-75	75	0.68	1.40
TLB-80	80	3.31	1.83
TLB-83	83	3.39	1.85
TLB-85	85	3.31	1.84
TLB-90	90	3.39	1.85

Appendix B. Hornos de Cal trench data

XRF (Results in wt.%)

Sample	Depth (cm)	Si	Ac	Ag	Al	Ba	Br	Ca	Cl	Cu	Fe	Fr	I	K
THC-06	2	9.909	0.034		3.146		0.075	51.421			2.386			2.625
THC-05	3	7.779	0.083					56.490			1.849	0.101	0.166	2.112
THC-04B	10	7.032			2.170			52.498		0.033	2.546			3.457
HC1804	13.5				2.367			50.364			1.964			1.963
THC-04A	20	9.510			2.667		0.044	49.957		0.048	1.877			1.562
HC1803	23.5							43.400			1.886			6.590
THC-03	40	6.144					0.344	39.077		0.057	1.903		0.090	8.459
HC1803	58							40.658			1.338			8.378
THC-02	68	9.909	0.034		3.146		0.075	51.421			2.386			2.625
HC1801	71				9.458			30.781			3.658			3.988
THC-01C	75	24.024			10.211		0.034	31.276		0.048	4.038			4.201
THC-01B	80	16.921			5.231		0.035	43.482		0.066	2.784			2.403
THC-01A	90	10.703			5.435		0.038	51.978			3.638			2.719

XRF (Results in wt.%)

Sample	Mg	Mn	P	Pb	Rb	S	Sc	Sm	Sr	Ti	V	Zn	Zr
THC-06	11.637	0.625	14.172	0.092		2.109			1.558	0.212			
THC-05	15.715	0.709	11.523	0.223		1.530			1.587	0.136			
THC-04B	9.103	0.594	10.968	0.093		9.562			1.603	0.304		0.037	
HC1804	11.269	0.628	15.947	0.860		1.963			1.694			0.033	
THC-04A	11.595	0.646	16.948			1.768	2.221		1.109			0.050	
HC1803	18.657	0.479	12.752			8.762			1.643				
THC-03	19.096	0.459	11.876			9.946	0.775		1.701			0.073	
HC1803	18.367	0.472	12.987			8.970			1.567				
THC-02	11.637	0.625	14.172	0.092		2.109			1.558	0.212			
HC1801	9.325	0.196	2.834			14.587			0.568			0.250	
THC-01C	9.171	0.190	2.206		0.022	13.310	0.375		0.403	0.417	0.021	0.022	0.029
THC-01B	10.942	0.150	1.963		0.012	15.242			0.681	0.217		0.023	
THC-01A	0.000	0.123	2.282		0.012	21.626	0.412		0.564	0.435		0.035	

Gastropods counting

Sample	Depth (cm)	Gastropods	Sample total weight (g)	Individuals per sample (#/g)
THC-06	2	21	795.93	0.026
THC-05	3	45	751.43	0.060
THC-04B	10	71	775.85	0.092
HC1804	13.5	63	750.3	0.084
THC-04A	20	57	575.59	0.099
HC1803	23.5	55	730.2	0.075
THC-03	40	15	618	0.024
HC1802	58	12	620.6	0.019
THC-02	68	6	1154.25	0.005
HC1801	71	51	1145.6	0.045
THC-01C	75	63	1134.47	0.056
THC-01B	80	102	1185.34	0.086
THC-01A	90	97	1045.01	0.093

Fish Bones and Shells

Sample	Depth (cm)	Fish Bones (g)	Shells (g)
THC-06	2	51.33	49.63
THC-05	3	38.20	48.16
THC-04B	10	26.97	65.32
HC1804	13.5	31.34	73.36
THC-04A	20	51.91	48.08
HC1803	23.5	50.02	46.42
THC-03	40	82.18	30.89
HC1802	58	85.56	29.11
THC-02	68	0.07	16.95
HC1801	71	4.09	66.38
THC-01C	75	3.87	63.53
THC-01B	80	2.12	87.04
THC-01A	90	1.27	92.81

FTIR analysis (wt.%)

Sample	Depth (cm)	Amph	Qz+Alb	Cal+Gy
THC-06	2	1.000	7.0	7.5
THC-05	3	2.000	6.0	10.0
THC-04B	10	1.500	9.0	9.5
HC1804	13.5			
THC-04A	20	0.500	8.0	13.5
HC1803	23.5			
THC-03	40	2.500	7.6	9.2
HC1802	58			
THC-02	68	2.000	10.0	5.8
HC1801	71			
THC-01C	75	0.500	6.5	9.5
THC-01B	80	8.571	13.0	17.0
THC-01A	90	3.000	9.5	15.0

Sphericity and roundness

Sample	Depth (cm)	Sphericity grade	Roundness grade
THC-06	2	-0.5	4.5
THC-05	3	-2.5	3.5
THC-04B	10	2.5	2.5
HC1804	13.5	2.5	2.5
THC-04A	20	4.5	2.5
HC1803	23.5	2.5	1.5
THC-03	40	2.5	1.5
HC1802	58	2.5	2
THC-02	68	4.5	4.5
HC1801	71	-2.5	3.5
THC-01C	75	-2.5	3.5
THC-01B	80	-2.5	4.5
THC-01A	90	-2.5	3.5

Sedimentological parameters (μm)

Sample	Depth (cm)	Mean	Sorting	Skewness	Kurtosis
THC-06	2	601.7	4.7	-0.354	0.708
THC-05	3	556.7	3.9	-0.69	0.601
THC-04B	10	420.1	5.4	-0.178	0.614
HC1804	13.5	510.0	5.2	-0.21	0.61
THC-04A	20	548.3	5.1	-0.296	0.605
HC1803	23.5	560.3	5.0	-0.763	0.680
THC-03	40	852.5	3.0	-1.057	0.77
HC1802	58	705.3	2.1	-0.564	0.79
THC-02	68	213.0	1.4	-0.126	0.963
HC1801	71	615.3	1.8	-1.245	1.152
THC-01C	75	1265.9	2.3	-1.401	1.215
THC-01B	80	1915.2	1.5	-1.183	0.384
THC-01A	90	2086.9	1.0	1.550	0.365

Organic vs. inorganic material

Sample	Depth (cm)	Organic (%)	Inorganic (%)	Ratio
THC-06	2	40	60	0.67
THC-05	3	65	35	1.86
THC-04B	10	40	60	0.67
HC1804	13.5	45	55	0.82
THC-04A	20	48	52	0.92
HC1803	23.5	75	25	3.00
THC-03	40	80	20	4.00
HC1802	58	85	15	5.67
THC-02	68	16	84	0.19
HC1801	71	65	35	1.86
THC-01C	75	59	41	1.44
THC-01B	80	79	21	3.76
THC-01A	90	64	36	1.78

Matrix sedimentological parameters (μm)

Sample	Depth (cm)	Mean*100	Sorting
THC-06	2	2.53	4.35
THC-05	3	2.35	3.55
THC-04B	10	2.68	2.50
HC1804	13.5	1.34	4.44
THC-04A	20	2.57	2.56
HC1803	23.5	2.35	3.55
THC-03	40	5.10	2.60
HC1802	58	3.06	4.41
THC-02	68	2.21	1.91
HC1801	71	1.05	7.75
THC-01C	75	1.10	3.25
THC-01B	80	2.68	2.50
THC-01A	90	5.92	2.20

Appendix C. Supplementary data

Supplementary data to this article can be found online at https://doi.org/10.1016/j.quascirev.2019.07.038.

References

Abad, M., Izquierdo, T., Cáceres, M., Bernárdez, E., Rodríguez-Vidal, J., 2019. Coastal boulder deposit as evidence of an ocean-wide prehistoric tsunami originated on the Atacama Desert coast (northern Chile). Sedimentology. https://doi.org/10.1111/sed.12570.

Abe, K., 1979. Size of great earthquakes of 1837–1974 inferred from tsunami data. J. Geophys. Res. 84 (B4), 1561–1568.

Angermann, D., Klotz, J., Reigber, C., 1999. Space-geodetic estimation of the Nazca-South America Euler vector. Earth Planet. Sci. Lett. 171, 329–334.

Arce, I., 1930/1997. Narraciones Históricas de Antofagasta. Fondo Nacional de Desarrollo Regional – Municipalidad de Antofagasta. Lama Industrial S.A., Antofagasta, 570 p. http://www.memoriachilena.gob.cl/602/w3-article-9292.html.

Atwater, B.F., 1987. Evidence for great earthquakes along the outer coast of Washington State. Science 236, 942–944.

Bagnold, R.A., 1954. Experiments on gravity-free dispersion of large solid spheres in a Newtonian fluid under shear. Roy. Soc. (Lond) Proc. A 225, 49–63.

Bahlburg, H., Nentwig, V., Kreutzer, M., 2017. The September 16, 2015 Illapel tsunami, Chile-Sedimentology of tsunami deposits at the beaches of La Serena and Coquimbo. Mar. Geol. 396, 43–53.

Barros, A., 2010. Tsunami en Bolivia y Perú: el terremoto y salida de mar del 9 de mayo de 1877 (Norte Grande, Chile). Rev. Cienc. Soc. 24, 73–93.

Béarez, P., Fuentes Mucherl, F., Rebolledo, S., Salazar Sutil, D., Olguín, L., 2016. Billfish foraging along the northern coast of Chile during the Middle Holocene (7400-5900 cal BP). J. Anhropological Archeol. 41, 185–195.

Beck, S., Barrientos, S., Kausel, E., Reyes, M., 1998. Source characteristics of historic earthquakes along the central Chile subduction zone. J. South Am. Earth Sci. 11, 115–129.

Bertaux, J., Fröhlich, F., Ildefonse, Ph, 1998. Multicomponent analysis of FTIR spectra: quantification of amorphous silica and crystallized mineral phases in synthetic and natural sediments. J. Sediment. Res. 68 (3), 440–447.

Blott, S., Pye, K., 2001. Gradistat: a grain size distribution and statistics package for the analysis of unconsolidated sediments. Earth Surf. Process. Landforms 26, 1237–1248.

Bozkurt, D., Rondanelli, R., Garreaud, R., Arriagada, A., 2016. Impact of warmer eastern tropical Pacific SST on the March 2015 Atacama floods. Mon. Weather Rev. 144, 4441–4460.

Cain, G., Goff, J., McFadgen, B.G., 2019. Prehistoric mass burials: did death come in waves? J. Archaeol. Method Theory 26, 714–754.

Carvajal, M., Contreras-López, M., Winckler, P., Sepúlveda, I., 2017. Meteotsunamis occurring along the southwest coast of south America during an intense storm. Pure Appl. Geophys. 174, 3313–3323.

Cisternas, M., Atwater, B.F., Torrejón, F., Sawai, Y., Machuca, G., Lagos, M., Eipert, A., Youlton, C., Salgado, I., Kamataki, T., Shishikura, M., Rajendran, C.P., Malik, J.K., Rizal, Y., Husni, M., 2005. Predecessors of the giant 1960 Chile earthquake. Nature 437, 404–407.

Clark, K., Cochran, U., Mazengarb, C., 2011. Holocene coastal evolution and evidence for paleotsunami from a tectonically stable region, Tasmania, Australia. Holocene 21, 883–895.

Comte, D., Pardo, M., 1991. Reappraisal of great historical earthquakes in the northern Chile and southern Peru seismic gaps. Nat. Hazards 4, 23–44.

Cruz, J., 1966. Fundación de Antofagasta y su primera década. Editorial Universitaria, Santiago, Chile, p. 133.

Dawson, A., 1994. Geomorphology effects of tsunami run up and backwash. Gemorphology 10, 83–94.

Delouis, B., Monfret, T., Dorbath, L., Pardo, M., Rivera, L., Comte, D., Cisternas, A., 1997. The M_w= 8.0 Antofagasta (Northern Chile) earthquake of 30 July 1995: a precursor to the end of the large 1877 gap. Bull. Seismol. Soc. Am. 87 (2), 427–445.

Deschamps, A., Lyon-Caen, H., Madariaga, R., 1980. Etude du tremblement de terre de Taltal, Chili (1966) à partir des ondes sismiques de longue période. Ann. Geophys. 36, 179–190.

Donnelly, J., Goff, J., Chagué-Goff, C., 2017. A record of local storms and trans-Pacific tsunamis, eastern Banks Peninsula, New Zealand. Holocene 27 (4), 496–508.

Dura, T., Engelhart, S., Vacchi, M., Horton, B.P., Kopp, R., Peltier, W.R., Bradley, S., 2016. The role of Holocene relative sea-level change in preserving records of subduction zone earthquakes. Curr. Clim. Change Rep. 2 (3), 86–100.

Dura, T., Horton, B.P., Cisternas, M., Ely, L., Hong, I., Nelson, A.R., Wesson, R.L., Pilarczyk, J.E., Parnell, A.C., Nikitina, D., 2017. Subduction zone slip variability during the last millennium, south-central Chile. Quat. Sci. Rev. 175, 112–137.

Ely, L.L., Cisternas, M., Wesson, R.L., Dura, T., 2014. Five centuries of tsunamis and land-level changes in the overlapping rupture area of the 1960 and 2010 Chilean earthquakes. Geology 42, 995–998.

Farías, M., Vargas, G., Tassara, A., Carretier, S., Baize, S., Melnick, D., Bataille, K., 2010. Land-level changes produced by the Mw 8.8 2010 Chilean earthquake. Science 329 (5994), 916.

Flores-Aqueveque, V., Alfaro, S., Munoz, R., Rutllant, J.A., Caquineau, S., Le Roux, J.P.,

Vargas, G., 2010. Aeolian erosion and sand transport over the Mejillones Pampa in the coastal Atacama Desert of northern Chile. Geomorphology 120 (3–4), 312–325.

Folk, R.L., Ward, W.C., 1957. A study in the significance of grain-size parameters. J. Sediment. Petrol. 27, 3–26.

Fuchs, C., 1878. Die vulkanischen Ereignisse des Jahre 1877. Mineral. Petrogr. Mittl. 1 (2), 106–136.

Galaz-Mandakovic, D., Owen, E., 2015. Hermanos Latrille: Impronta del Desierto. Pau (Francia) Tocopilla (Litoral Boliviano-Norte de Chile). Retruécanos Ediciones, Antofagasta, Chile.

Geinitz, E., 1878/2010. Das Erdbeben Von Iquique Am 9 Mai 1877. Kessinger Publishing, Lakefish, Montana, USA.

Goff, J., Chagué-Goff, C., Nichol, S., 2001. Paleotsunami deposits: a New Zealand perspective. Sediment. Geol. 143, 1–6.

Goff, J., McFadgen, B.G., Chagué-Goff, C., 2004. Sedimentary differences between the 2002 easter storm and the 15th-century Okoropunga tsunami, southeastern north Island, New Zealand. Mar. Geol. 204, 235–250.

Goff, J., Nichol, S.L., Chagué-Goff, C., Horrocks, M., McFadgen, B., Cisternas, M., 2010. Predecessor to New Zealand's largest historic trans-South Pacific tsunami of 1868 AD. Mar. Geol. 275, 155–165.

Goff, J., Chagué-Goff, C., Dominey-Howes, D., McAdoo, B., Cronin, S., Bonté-Grapetin, M., Nichols, S., Horrocks, M., Cisternas, M., Lamarche, G., Pelletier, B., Jaffe, B., Dudley, W., 2011. Palaeotsunamis in the Pacific Islands. Earth Sci. Rev. 107, 141–146.

Goff, J., Chagué-Goff, C., Nichol, S., Jaffe, B., Dominey-Howes, D., 2012. Progress in palaeotsunami research. Sediment. Geol. 243–244, 70–88.

Goff, J., Goto, K., Chagué, C., Watanabe, M., Gadd, P.S., King, D.N., 2018. New Zealand's most easterly palaeotsunami deposit confirms evidence for major trans-Pacific event. Mar. Geol. 404, 158–173.

González-Alfaro, J., Vargas, G., Ortlieb, L., González, G., Ruiz, S., Báez, J.C., Mandeng-Yogo, M., Caquineau, S., Álvarez, G., Del Campo, F., Del Río, I., 2018. Abrupt increase in the coastal uplift and earthquae rate since ~ 40 ka at the northern Chile seismic gap in the Central Andes. Earth Planet. Sci. Lett. 502, 32–45.

Guzmán, N., Saá, S., Ortlieb, L., 1998. Catálogo descriptivo de los moluscos litorales (Gastropoda y Pelecypoda) de la zona de Antofagasta, 23°S (Chile). Descriptive catalogue of nearchore molluscs (gastropoda and Pelicypoda) from Antofagasta area, 23°S (Chile). Estud. Oceanol. 17, 17–86.

Herrera, C., Custodio, E., 2014. Origin of waters from small springs located at the northern coast of Chile, in the vicinity of Antofagasta. Andean Geol. 41 (2), 314–341.

Houston, J., 2006. Variability of precipitation in the Atacama Desert: its causes and hydrological impact. Int. J. Climatol. 26, 2181–2198.

Jaffe, B., Goto, K., Sugawara, D., Richmond, B., Fujino, Sh, Nishimura, Y., 2012. Flow speed estimated by inverse modeling of sandy tsunami deposits: results from the 11 March 2011 tsunami on the coastal plain near the Sendai Airpot, Honshu, Japan. Sediment. Geol. 282, 90–109.

Khan, N.S., Ashe, E., Shaw, T.A., Vacchi, M., Walker, J., Peltier, W.R., Kopp, R., Horton, B.P., 2015. Holocene relative sea-level changes from near-, intermediate-, and far-field locations. Curr. Clim. Change Rep. 1, 247–262.

Kausel, E., 1986. Los Terremotos de Agosto de 1868 y Mayo de 1877 que Afectaron el Sur del Peru y Norte de Chile. Boletín de la Academia Chilena de Ciencias 3, 8–12.

Kelsey, H.M., Witter, R.C., Hemphill-Haley, E., 2002. Plate-boundary earthquakes and tsunamis of the past 5500 yr. Sixes River estuary, southern Oregon. Geol. Soc. Am. Bull. 114 (3), 298–314.

Lambeck, K., Rouby, H., Purcell, A., Sun, Y., Sambridge, M., 2014. sea level and global ice volumens from the last Glacial maximum to the Holocene. Proc. Natl. Acad. Sci. 111 (43), 15296–15303.

Le Roux, J.P., 2003. Can dispersive pressure cause inverse grading in grain flows?—discussion. J. Sediment. Res. 73, 331–332.

Le Roux, J.P., Vargas, G., 2005. Hydraulic behavior of tsunami backflows: insights from their modern and ancient deposits. Environ. Geol. 49 (1), 65–75.

Lomnitz, C., 2004. Major earthquakes of Chile: a historical survey, 1535–1960. Seismol. Res. Lett. 75 (3), 368–378.

Métois, M., Vigny, C., Socquet, A., 2016. Interseismic coupling, megathrust earthquakes and seismic Swarms along the Chilean subduction zone (38°–18°S). Pure Appl. Geophys. 173, 1431–1449.

Middleton, G.V., 1967. Experiments on density and turbidity currents—III: deposition of sediment. Can. J. Earth Sci. 3, 523–546.

Moore, A., Goff, J., McAdoo, B., Fritz, H., Gusman, A., Kalligeris, N., Kalsum, K., Susanto, A., Suteja, D., Synolakis, C., 2011. Sedimentary deposits from the 17 july western Java tsunami. Indonesia: use of grain size analysis to assess tsunami flow depth. Speed. And traction carpet characteristics. Pure Appl. Geophys. 168, 1951–1961.

Morton, R., Gelfenbaum, G., Jaffe, B., 2007. Physical criteria for distinguishing sandy tsunami and storm deposits using modern examples. Sediment. Geol. 200, 184–207.

Morton, R., Goff, J., Nichol, S., 2008. Hydrodynamic implication of textural trends ina sand deposits of the 2004 tsunami in Sri Lanka. Sediment. Geol. 207, 56–64.

Nelson, A.R., Shennan, I., Long, A.J., 1996. Identifying coseismic subsidence in tidal wetland stratigraphic sequences at the Cascadia subduction zone of western North America. J. Geophys. Res. 101, 6115–6135.

New Zealand Palaeotsunami Database, 2018. https://ptdb.niwa.co.nz. (Accessed 18 June 2018).

Nichols, G., 2009. Sedimentology and Stratigraphy, second ed. Wiley-Blackwell.

456p.

Nichol, S.L., Goff, J.R., Devoy, R.J.N., Chagué-Goff, C., Hayward, B., James, I., 2007. Lagoon subsidence and tsunami on the west coast of New Zealand. Sediment. Geol. 200, 248–262.

Olguín, L., Flores, C., Salazar, D., 2015. Aprovechamiento humano de moluscos marinos en conchales arqueológicos del Holoceno Temprano y Medio (12.000-5.000 años cal A.P.). Costa meridional del Desierto de Atacama. Chile. In: Salomon, H., Zubimendi, M.A. (Eds.), Arqueología y malacología: abordajes metodológicos y casos de estudio en el Cono Sur. Fundación de Historia Natural Félix de Azara, Argentina, pp. 13–34.

Ortlieb, L., Barrientos, S., Guzmán, N., 1996. Coseismic coastal uplift and coralline algae record in northern Chile: the 1995 Antofagasta earthquake case. Quat. Sci. Rev. 15 (8–9), 949–960.

Ortlieb, L., Vargas, G., Saliège, J.-F., 2011. Marine radiocarbon reservoir effect along the northern Chile–southern Peru coast (14–24°S) throughout the Holocene. Quat. Res. 75, 91–103.

Plafker, G., Savage, J.C., 1970. Mechanism of the Chilean earthquakes of may 21 and 22, 1960. Geol. Soc. Am. Bull. 81, 1001–1030.

Plafker, G., Lajoie, K.R., Rubin, M., 1992. Determining recurrence intervals of great subduction zone earthquakes in southern Alaska by radiocarbon dating. In: Radiocarbon after Four Decades. Springer, New York, pp. 436–453.

Rebolledo, S., Béarez, P., Salazar, D., Fuentes, F., 2016. Maritime fishing during the middle Holocene in the hyperarid coast of the Atacama Desert. Quat. Int. 391, 3–11.

Ruiz, S., Madariaga, R., 2018. Historical and recent large megathrust earthquakes in Chile. Tectonophysics 733, 37–56.

Rundel, P.W., Dillon, M.O., Palma, B., Mooney, H.A., Gulmon, S.L., 1991. The phyto-geography and ecology of the coastal Atacama and Peruvian Deserts. Aliso J. System. Evolut. Bot. 13, 1–49.

Salazar, D., Figueroa, V., Andrade, P., Salinas, H., Olguín, L., Power, X., Rebolledo, S., Parra, S., Orellana, H., Urrea, J., 2015. Cronología y Organización Económica de las Poblaciones Arcaicas de la Costa de Taltal. Estud. Atacameños 50, 07–46.

Salazar, D., Arenas, C., Andrade, P., Olguín, L., Torres, J., Flores, C., Vargas, G., Rebolledo, S., Borie, C., Sandoval, C., Silva, C., Delgado, A., Lira, N., Robles, C., 2018. From the use of space to territorialisation during the early Holocene in taltal, coastal Atacama Desert, Chile. Quat. Int. 473, 225–241.

Satake, K., Atwater, B.F., 2007. Long-term perspectives on giant earthquakes and tsunamis at subduction zones. Annu. Rev. Earth Planet Sci. 35, 349–374.

Sawai, Y., 2001. Episodic emergence in the past 3000 years at the Akkeshi estuary, Hokkaido, northern Japan. Quat. Res. 56, 231–241.

Schulte, P., Smit, J., Deutsch, A., Salge, T., Friese, A., Beichel, K., 2011. Tsunami backwash deposits with Chicxulub impact ejecta and dinosaur remains from the Cretaceous–Palaeogene boundary in the La Popa Basin, Mexico. J. Int. Associat. Sedimentol. 59, 737–765.

Schurr, B., Asch, G., Hainzl, S., Bedford, J., Hoechner, A., Palo, M., Wang, R., Moreno, M., Bartsch, M., Zhang, Y., Oncken, O., Tilmann, F., Dahm, F., Victor, P., Barrientos, S., Vilotte, J.P., 2014. Gradual unlocking of plate boundary controlled initiation of the 2014 Iquique earthquake. Nature 512, 299–302.

SHOA (Servicio Hidrográfico y Oceanográfico de la Armada de Chile), 2010. Registro de los principales tsunamis que han afectado a la costa de Chile, vols. 1–6. http://www.shoa.cl/s3/servicios/tsunami/data/tsunamis_historico.pdf.

SHOA (Servicio Hidrográfico y Oceanográfico de la Armada de Chile), 2012. Cartas de Inundación por Tsunami (CITSU), Puerto Taltal. Tocopilla (2012), Mejillones (2012), Antofagasta (2013), Chañaral (2014), Huasco (2015), Coquimbo-La Ser-ena (2015). http://www.shoa.cl/php/citsu.php.

Silgado, E., 1985. Terremotos destructivos en América del Sur: 1530-1894. Centro Regional de Sismología para América del Sur (CERESIS) 10, 328 p.

Slootman, Simpson, G., Castelltort, S., Boer, P., 2018. Geological record of marine tsunami backwash: the role of the hydraulic jump. Depos. Rec. 4 (1), 59–77.

Spiske, M., Piepenbreier, J., Benavente, C., Bahlburg, H., 2013. Preservation potential of tsunami deposits on arid siliciclastic coasts. Earth Sci. Rev. 126, 58–73.

Stuiver, M., Reimer, P.J., Reimer, R.W., 2018. CALIB 7.1 [WWW program] at. http://calib.org. (Accessed 19 June 2018).

Switzer, A., Pucillo, K., Haredy, R., Jones, B., Bryant, E., 2005. Sea level, storm, or tsunami: enigmatic sand sheet deposits in a sheltered coastal embayment from southeastern New South Wales. Australia. J. Coast. Res. 21, 655–663.

Tsuji, Y., 2013. Catalog of distant tsunamis reaching Japan from Chile and Peru. Rep. Tsunami Eng. 30, 61–68.

Vargas, G., Ortlieb, L., Rutllant, J., 2000. Aluviones historicos en Antofagasta y su relacion con eventos El Niño/Oscilacion del Sur. Rev. Geol. Chile 27, 157–176.

Vargas, G., Ortlieb, L., Chapron, E., Valdes, J., Marquardt, C., 2005. Paleoseismic in-ferences from a high-resolution marine sedimentary record in northern Chile (23°S). Tectonophysics 399, 381–398.

Vargas, G., Rutllant, J., Ortlieb, L., 2006. ENSO tropical-extratropical climate tele-connections and mechanisms for Holocene debris flows along the hyperarid coast of western South America (17°-24°S). Earth Planet. Sci. Lett. 249, 467–483.

Vargas, G., Farías, M., Carretier, S., Tassara, A., Baize, S., Melnick, D., 2011. Coastal uplift and tsunami effects associated to the 2010 M_w 8.8 earthquake in central Chile. Andean Geol. 38 (1), 219–238.

Williams, S., Goff, J., Prasetya, G., Cheung, K.F., Chagué-Goff, C., Davies, T., Wilson, T., 2011. Characterizing diagnostic proxies for identifying palaeotsunamis in a tropical climatic regime. In: Samoan Islands. MTS/IEEE Oceans 2011 Conference. Kona, Hawaii, 10 pp.

Witter, R.C., Kelsey, H.M., Hemphill-Haley, E., 2003. Great Cascadia earthquakes and tsunamis of the past 6700 years, Coquille River estuary, southern coastal Ore-gon. Geol. Soc. Am. Bull. 115 (10), 1289–1306.